BEILSTEIN JOURNAL OF NANOTECHNOLOGY

Graphene and beyond

Edited by Giridhar U. Kulkarni and C.N.R. Rao

Imprint

Beilstein Journal of Nanotechnology
www.bjnano.org
ISSN 2190-4286
Email: journals-support@beilstein-institut.de

The *Beilstein Journal of Nanotechnology* is published by the Beilstein-Institut zur Förderung der Chemischen Wissenschaften.

Beilstein-Institut zur Förderung der
Chemischen Wissenschaften
Trakehner Straße 7–9
60487 Frankfurt am Main
Germany
www.beilstein-institut.de

BEILSTEIN JOURNAL OF NANOTECHNOLOGY

Simple synthesis of nanosheets of rGO and nitrogenated rGO

Pallellappa Chithaiah[1,2], Madhan Mohan Raju[1], Giridhar U. Kulkarni[1] and C. N. R. Rao*[2]

Full Research Paper

Open Access

Address:
[1]Centre for Nano and Soft Matter Sciences, Jalahalli, Bangalore, 560013, India and [2]New Chemistry Unit, International Centre for Materials Science, Jawaharlal Nehru Centre for Advanced Scientific Research, Jakkur P.O., Bangalore, 560064, India

Email:
C. N. R. Rao* - cnrrao@jncasr.ac.in

* Corresponding author

Keywords:
nanosheets; nitrogenated reduced graphene oxide (N-rGO); reduced graphene oxide (rGO); supercapacitors; thermal decomposition

Beilstein J. Nanotechnol. **2020,** *11,* 68–75.
doi:10.3762/bjnano.11.7

Received: 12 October 2019
Accepted: 14 December 2019
Published: 07 January 2020

This article is part of the thematic issue "Graphene and beyond".

Associate Editor: A. Gölzhäuser

Abstract

A green and facile approach has been developed for the large-scale synthesis of nanosheets of reduced graphene oxide (rGO) and nitrogenated reduced graphene oxide (N-rGO). This has been achieved by direct thermal decomposition of sucrose and glycine at 475 °C in ca. 7 minutes, respectively. The present protocols for synthesizing rGO and N-rGO are simple and environmentally friendly as we do not use any harmful reagents, metal catalysts and solvents. Along with that, this method offers an inexpensive route with high yields to prepare rGO with a high nitrogen content (20–25 atom %). To further improve the properties of the synthesized rGO sheets, hydrogen treatment has been carried out to reduce the oxygen functional groups. Cyclic voltammograms and charge–discharge experiments have been carried out to understand the supercapacitor behavior of rGO and hydrogen treated (H-rGO) samples.

Introduction

Graphene, the one atom thick two-dimensional material of sp^2-hybridized carbon atoms has attracted much attention after its discovery [1,2]. It is a fascinating material used in various applications owing to its excellent electrical, optical, mechanical and thermal properties [3-5]. It has a unique electronic structure with a linear dispersion of Dirac electrons. Graphene oxide (GO) and reduced graphene oxide (rGO) are chemically modified forms of graphene, which are extensively studied in the field of science and engineering. Reduced graphene oxide has attracted significant interest due to its similarities to pristine graphene. It behaves like a semimetal or a semiconductor and is therefore used in a variety of hybrid systems such as batteries [6], electrodes [7] and photodetectors [8].

In 1958, Hummer and Offeman developed a chemical method to synthesize graphene oxide by acid treatment of graphite [9]. The graphene oxide thus obtained contains oxygen functional groups (–CO–, –COC–) on the surface and edges of the carbon sheet, which lead to a disruption of the conjugated network and the flow of charge carriers is reduced by several orders of magnitude [10]. Up to now, several methods including chemical vapor deposition [11-13], arc discharge [14], aerosol pyrolysis [15], mechanical exfoliation [1], solvothermal [16], hydrothermal synthesis [17], laser reduction of graphite oxide [18,19], and photo thermal deoxygenation of graphene oxide by camera flash have been developed to reduce the oxygen content of GO in order to restore the conjugated network [20]. Recently, a well-known chemical reduction method has been developed to obtain rGO through the reduction of exfoliated GO using various reducing agents such as hydrazine or dimethylhydrazine [21], $NaBH_4$ [22], hydroquinone [23], or glucose [24]. However, these methods have not yet turned into a global strategy to prepare pure rGO in a scalable fashion. Therefore, searching for a new synthetic approach to obtain pure phases of rGO is a highly desirable and great challenge for materials chemists.

Herein, we report for the first time a generic and rapid method for the synthesis of rGO nanosheets by direct thermal decomposition of sugar, without the use of any solvents, metal catalysts, reagents and hazardous chemicals. Similarly, N-rGO nanosheets have also been synthesized using glycine as precursor.

Results and Discussion

The typical XRD patterns of rGO and N-rGO nanosheets are shown in Figure 1. The XRD pattern of the as-prepared rGO (Figure 1a) exhibits a broad peak at 23.5° corresponding to an interlayer *d*-spacing of 0.378 nm. The XRD pattern of N-rGO (Figure 1b) shows a diffraction peak at 25.8° corresponding to an interlayer d spacing of 0.345 nm. From the XRD patterns, it is observed that the peak commonly obtained for GO around 2θ of 10.3° does not appear indicating that the precursors were directly converted into rGO and N-rGO nanosheets.

Figure 2 shows the Raman spectra of the rGO and N-rGO nanosheets. The Raman spectrum of the rGO sample (Figure 2a) shows D, G and 2D band at, respectively, 1362, 1594 and 2880 cm^{-1}. The spectrum of the N-rGO sample (Figure 2b) shows D, G and 2D band at, respectively, at 1354, 1581, and 2843 cm^{-1}. The D-band is associated with the breathing modes of six-membered carbon rings that are activated by defects and structurally disordered, and the G-band originates from in-plane vibrations of sp^2-hybridized carbon atoms in the rGO domains. The 2D-band is the second order of the D-band. The Raman results are consistent with previous reports [5].

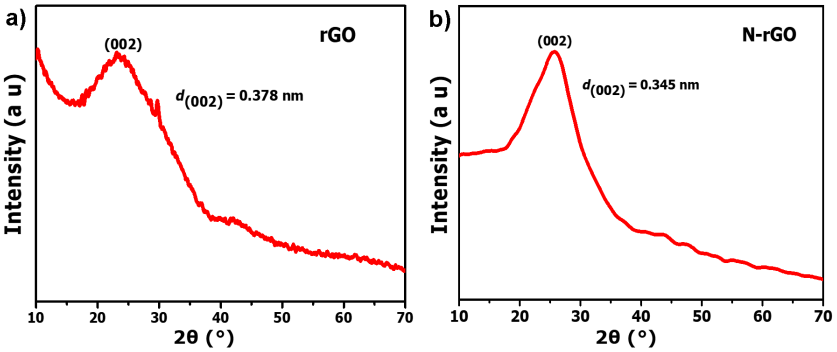

Figure 1: XRD patterns of (a) rGO and (b) N-rGO nanosheets.

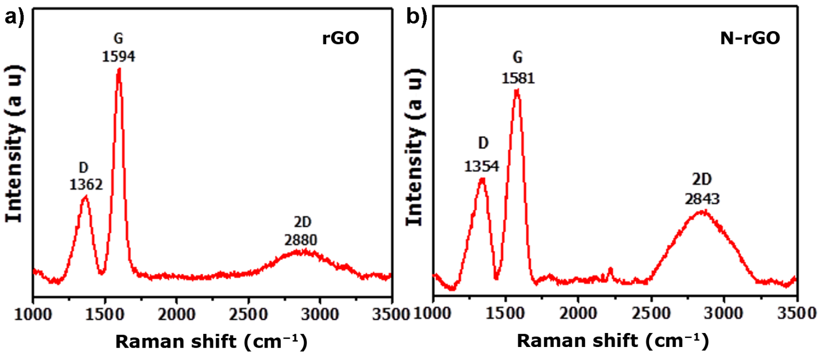

Figure 2: Raman spectra of (a) rGO and (b) N-rGO nanosheets.

Thermogravimetric analysis (TGA) was carried out to investigate the thermal stability of the rGO and N-rGO nanosheets. The study was performed in an oxygen atmosphere at a heating rate of 3 °C·min^{-1}. The results of rGO and N-rGO are shown in Figure 3a and Figure 3b, respectively. The initial weight losses occurring for rGO and N-rGO between room temperature and ca. 150 °C can be attributed to the evaporation of physically adsorbed water molecules.

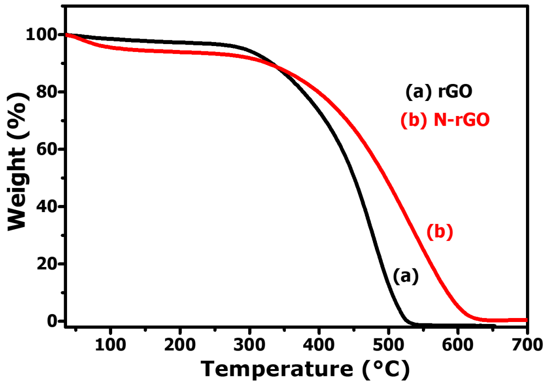

Figure 3: TGA curves of (a) rGO and (b) N-rGO nanosheets.

The second weight loss (93.4%) for rGO occurring between 350 and 540 °C can be ascribed to the decomposition of the carbon network. For N-rGO nanosheets, a significant weight loss occurs in the temperature range between 400 and 625 °C, due to the decomposition of N-rGO. The results are consistent with the previous reports suggested in the literature [25,26].

Typical SEM and TEM images of rGO at different magnifications are shown in Figure 4a,b. The low-magnification SEM image of the prepared rGO sample is composed of a large number of nanosheets, as shown in Figure 4a. The high-magnification SEM image (Figure 4b) shows that the nanosheets possess a smooth surface and are loosely stacked.

Energy-dispersive X-ray spectroscopy (EDS) was also measured to determine the chemical composition of rGO. Result from EDS shows (Figure 4c) that the product contains only C and O. The atomic fractions of C and O are found to be 76.03% and 23.97%, respectively, as shown in the inset of Figure 4c. The TEM image shown in Figure 4d indicates that the rGO sample is comprised of nanosheets with a smooth surface. The TEM image is in accordance with the SEM image (Figure 4b) of the sample. The selected area electron diffraction (SAED) pattern of the rGO sheets (inset in Figure 4d) shows a hexagonal pattern indicating the crystalline nature of the rGO sheets.

SEM images of N-rGO are shown in Figure 5a,b. The SEM images of N-rGO show morphological features that are similar

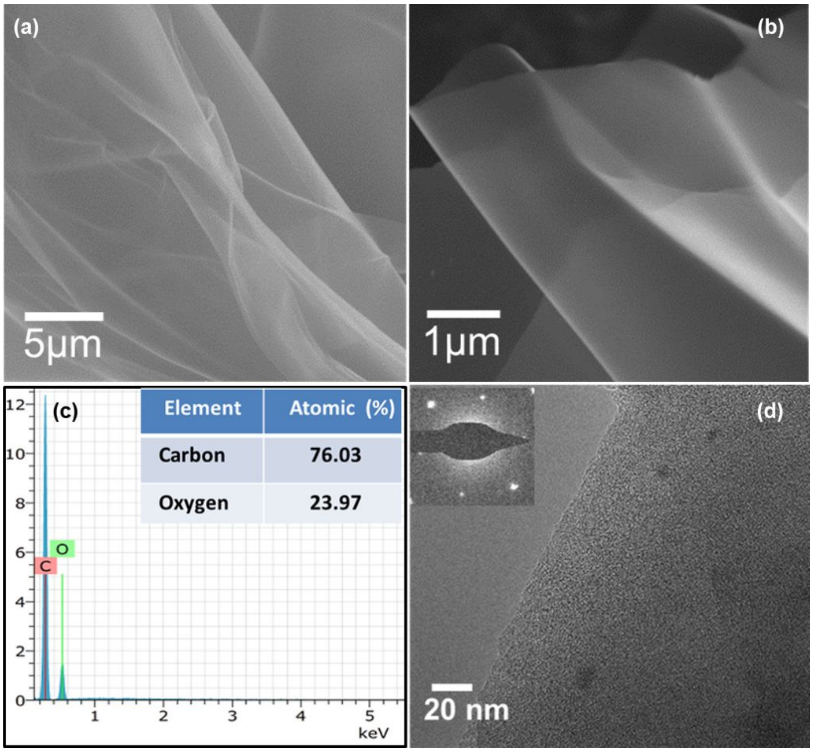

Element	Atomic (%)
Carbon	76.03
Oxygen	23.97

Figure 4: (a, b) SEM images, (c) EDS pattern and chemical composition (inset), and (d) TEM image and SAED pattern (inset) of the rGO nanosheets.

to those of rGO. EDS shows (Figure 5c) that the product contains only C, N and O. The atomic fractions of C, N and O are found to be 66.26%, 21.94%, and 11.81%, respectively, as shown in the inset of Figure 5c. The presence of nitrogen in the as N-rGO sample is also confirmed by the estimation of N content via CHNS analysis. The result shows that the weight percentage of N element in the N-rGO nanosheets is found to be approximately 20%, and this is in good agreement with the EDS results.

The TEM image in Figure 5d clearly shows that the N-rGO sample is composed of nanosheets with a smooth surface. The SAED pattern of the N-rGO sheet (inset in Figure 5d) shows a hexagonal pattern suggesting the crystalline nature of the synthesized N-rGO sheets.

AFM height images of as-prepared rGO and N-rGO nanosheets are displayed in Figure 6a and Figure 6b, respectively. The rGO and N-rGO nanosheets are flat with an average thickness of

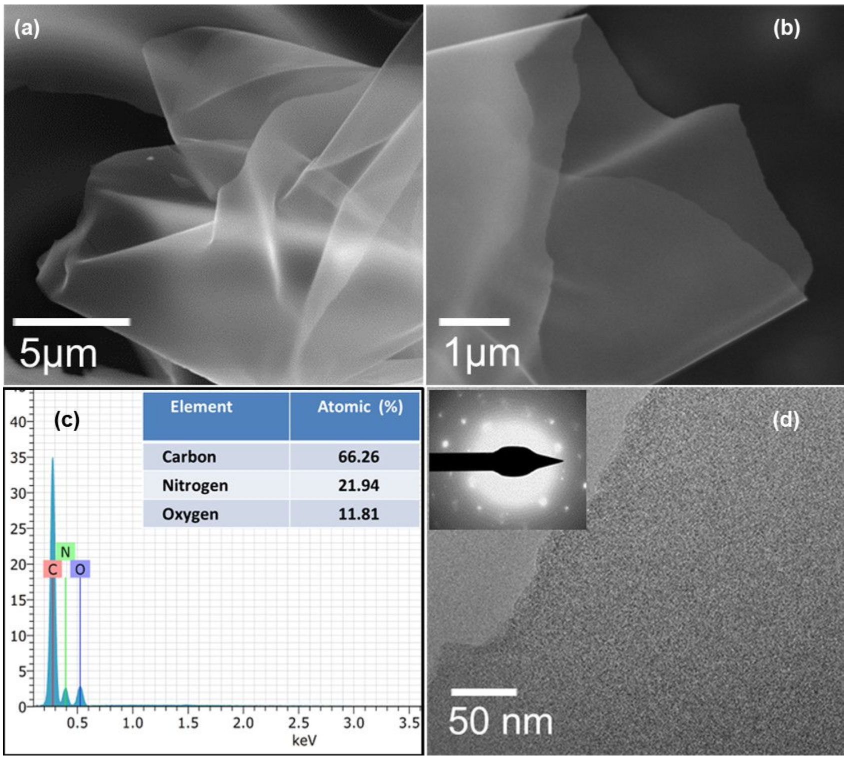

Element	Atomic (%)
Carbon	66.26
Nitrogen	21.94
Oxygen	11.81

Figure 5: (a, b) SEM images, (c) EDS pattern and chemical composition (inset), and (d) TEM image and SAED pattern (inset) of the N-rGO nanosheets.

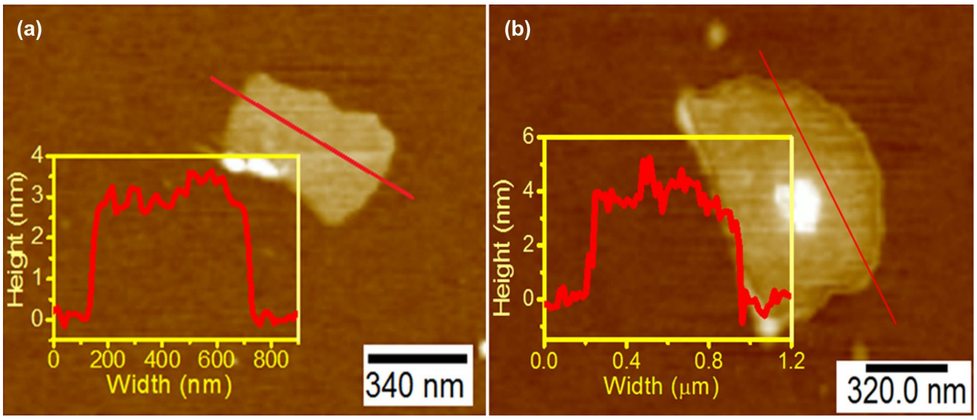

Figure 6: AFM images of (a) rGO and (b) N-rGO nanosheets.

about 3 nm and 3.5 nm, respectively, with their lateral dimension in the range of several hundred nanometers.

The experimental process and the digital photographs of rGO and N-rGO products are shown in Figure 7. Sucrose consists of one molecule of glucose and one molecule of fructose. The sucrose molecule contains –OH, -CH_2OH, and –C–O–C– functional groups. At a temperature of 475 °C in a pre-heated muffle furnace, within a short period of time, sucrose undergoes covalent cross-linking reactions yielding the formation of C–C and C=C bonds through the removal of water and CO_2. It is finally converted into a lightweight fluffy kind of material called graphene oxide nanosheets. The product was left in a furnace for ca. 7 min to get the pure phase without any impurities. The fraction of oxygen in the prepared sample is ca. 24 atom %, as measured with EDS, and the XRD pattern of the sample shows a broad peak around 23.5°. Therefore, the obtained product can be considered to be reduced graphene oxide. Similarly, glycine also undergoes a cross-linking reaction with the removal of CO_2 and H_2O leading to the formation of nitrogen-doped reduced graphene oxide nanosheets. For comparison we have also synthesized rGO sheets at 400 and 600 °C as well. The corresponding XRD patterns, Raman spectra and SEM images are given in Figure S1 and Figure S2, respectively, in Supporting Information File 1.

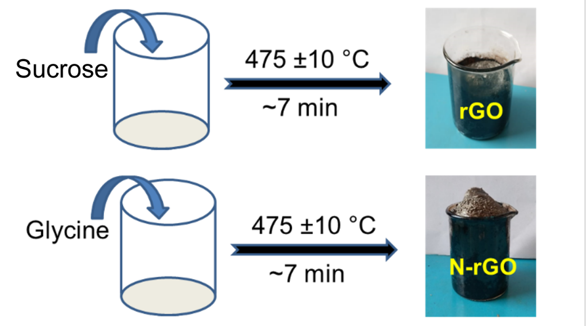

Figure 7: Schematic diagram of the formation of rGO and N-rGO nanosheets.

In order to understand the supercapacitor behavior of rGO and H-rGO (hydrogen-treated rGO) samples, we have carried out cyclic voltammetry and CD experiments with three-electrode system using 1 M H_2SO_4 as electrolyte (Figure 8).

CV curves of rGO and H-rGO at different scan rates from 5 to 200 $mV \cdot s^{-1}$ vs Hg/Hg_2SO_4 are shown in Figure 8a and

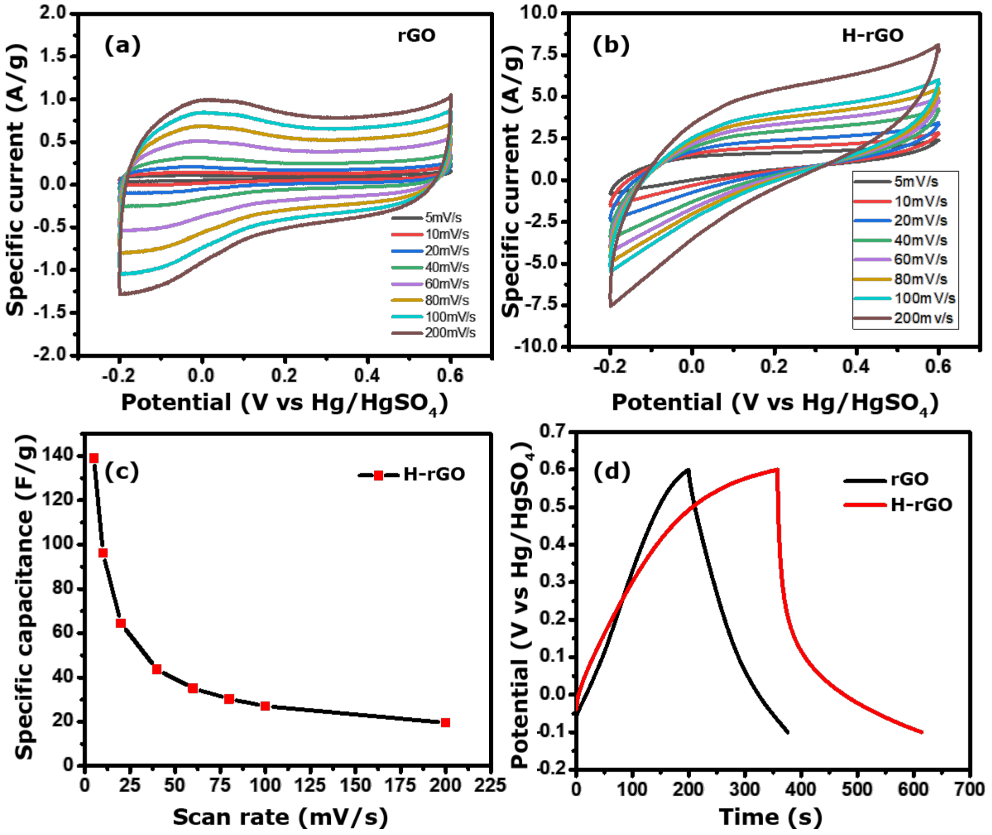

Figure 8: CV curves for (a) rGO and (b) H-rGO samples at different scan rates; (c) specific capacitance for H-rGO at scan rates from 5 to 200 $mV \cdot s^{-1}$; (d) charge–discharge curves of rGO and H-rGO at a current density of 0.5 $A \cdot g^{-1}$.

Figure 8b, respectively. These curves show increase in current density with decreasing scan rate, suggesting that the samples have ideal capacitor characteristics. However, the H-rGO sample shows a higher current density and hence a higher specific capacitance than rGO. The calculated specific capacitance values from the CV of the rGO and H-rGO electrodes at 5 mV·s^{-1} are 7 (not shown) and 139 F·g^{-1}, respectively. We have checked the rate capability of the working electrode at different scan rates of 10, 20, 40, 60, 80, 100, and 200 mV·s^{-1} and observed that the specific capacitance values were 96, 64, 43, 35, 30, 27 and 19 F·g^{-1}, respectively (Figure 8c). For comparison, the charge–discharge (CD) curves for rGO and H-rGO nanosheets were recorded at a current density of 0.5 A·g^{-1} in 1 M H_2SO_4 (Figure 8d). The specific capacitance values obtained from the CD curves at a current density of 0.5 A·g^{-1} for rGO and H-rGO were 137 and 203 F·g^{-1}, respectively. The CD curve of H-rGO also shows a higher specific capacitance compared to rGO. The higher specific capacitance of H-rGO is attributed an increased conductivity due to the reduced number of functional groups after hydrogen reduction of the rGO sample. After 1000 cycles, the H-rGO sample shows 73% retention, implying that the H-rGO has excellent stability (Figure 9). We compared our result with other materials reported recently (Table 1). For conductivity measurements, the H-rGO sample was dispersed in ethanol and drop-cast on a gold gap electrode. The average resistance measured using a Keithley source meter is ca. 4 MΩ. The corresponding electrical conductivity obtained for H-rGO is ca. 0.068 S/m.

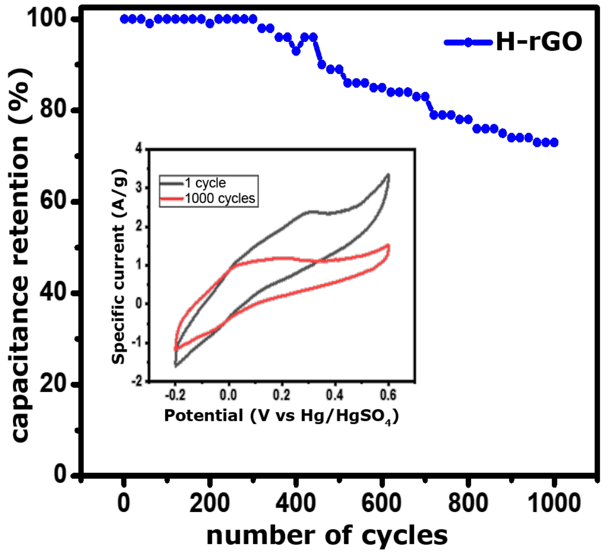

Figure 9: Cycling stability of H-rGO.

Conclusion

In conclusion, we present a very simple and efficient method for the successful synthesis of nanosheets of rGO and of rGO with high nitrogen content by the thermal decomposition of sucrose and glycine. We measured the specific capacitance and carried out charge–discharge experiments. The rGO nanosheets that were hydrogen-treated (H-rGO) showed good supercapacitor behavior.

Experimental

Preparation of rGO and N-rGO nanosheets

Sucrose in the form of granulated table sugar from a retail store and analytical grade glycine from Sigma-Aldrich were purchased and used without further purification. Reduced graphene oxide (rGO) was prepared by using granulated table sugar. 2.0 g of sucrose was taken in a 100 mL borosil glass beaker. Then, the beaker was directly introduced into the preheated muffle furnace maintained at 475 ± 10 °C in oxygen atmosphere. The sugar undergoes dehydration, producing a black foam in ca. 7 min. Finally, the resultant product was collected for further analysis. A similar procedure was followed to prepare N-rGO using glycine as precursor.

Hydrogen treatment of rGO nanosheets

Hydrogen-treated reduced graphene oxide (H-rGO) was obtained as follows. 0.5 g of the rGO sample was taken in a ceramic boat and placed in a tube furnace. The sample was heated at 700 °C for 1 h in a continuous flow of H_2/Ar gas (5% hydrogen gas with Argon). After the reaction, the temperature was allowed to cool down to room temperature naturally. The resulting product was collected and used for the electrochemical supercapacitor measurements. The obtained results were compared with the as-synthesized rGO nanosheets.

Table 1: Comparison of the specific capacitance of H-rGO sheets with reported values.

material	structure	specific capacitance (F·g^{-1})	reference
porous electrochemically rGO	nanosheets	81 ± 3	[27]
graphene oxide	nanosheets	121	[28]
RGO/H_xPO_y	nanosheets	101	[29]
RGO	nanosheets	90	[29]
H-rGO	nanosheets	139	this work

Materials characterization

The samples were characterized using transmission electron microscopy (TEM), atomic force microscopy (AFM), X-ray diffraction (XRD) and thermogravimetric analysis (TGA). X-ray diffraction patterns of the samples were collected in the range of 10–70° (2θ) using a Bruker D8 diffractometer with a Cu Kα source (λ = 0.154178 nm). The morphology of the samples was examined using a Tescan Mira3 field-emission scanning electron microscope (FESEM) equipped with an energy-dispersive X-ray spectroscopy (EDS). The TEM, HRTEM images and SAED patterns were obtained on a TALOS F200S G2, 200 kV FEG, and a CMOS camera (4k × 4k). The TEM samples were prepared by suspending the samples in ethanol, using an ultrasonic bath, and subsequent dripping of the suspension on the grid and drying. Raman spectra of the samples were recorded using a Jobin Yvon LabRam HR spectrometer with a 514 nm Ar laser. Thermogravimetric analysis of the samples was carried out in an oxygen flow with a heating rate of 3 $°C \cdot min^{-1}$ using a Mettler-Toledo-TG-850 apparatus. AFM measurements were performed using a CP2 atomic force microscope.

Electrode preparation and electrochemical characterization

The catalyst inks of as-synthesized rGO and reduced graphene oxide H-rGO were prepared by ultrasonication separately. A mixture of 4.0 mg rGO and 0.025 wt % (5 μL) of Nafion in 0.4 mL of dimethylformamide (DMF) was sonicated until a homogeneous dispersion was obtained. 3 μL catalyst ink was taken and drop-cast onto a glassy carbon electrode, which was allowed to dry at room temperature. A similar procedure was followed to prepare the H-rGO electrode. The electrochemical studies, including cyclic voltammetry (CV) and chronopotentiometry charge–discharge (CD), were carried out at room temperature in 1 M H_2SO_4 solution in a standard three-electrode cell using an electrochemical workstation CHI 660E. This system consists of a glassy carbon working electrode (3 mM), a platinum wire counter electrode and a Hg/Hg_2SO_4 reference electrode with 1 M H_2SO_4 electrolyte. The specific capacitance (SC) of rGO and H-rGO was calculated from CV curves, according to Equation 1:

$$\mathrm{SC} = \int I\mathrm{d}V \Big/ 2\nu m \cdot \Delta V, \tag{1}$$

where $\int I\mathrm{d}V$ is the area under the CV curve, m is the mass of the active material, ν is the potential scan rate (V/s), and ΔV is the potential window. We have also calculated the specific capacitance from CD curves using Equation 2:

$$\mathrm{SC} = It \big/ m \cdot \Delta V, \tag{2}$$

where I is the current, t is the time of the discharge cycle, m is the mass of the active material, and ΔV is the potential window of the discharge cycle.

Supporting Information

Supporting Information File 1

Additional experimental data.
[https://www.beilstein-journals.org/bjnano/content/supplementary/2190-4286-11-7-S1.pdf]

Acknowledgements

PC thanks CeNS for fellowship and JNCASR for facilities. The authors acknowledge the TEM Facility, funded by TPF Nanomission, GoI project at CeNS, Bengaluru. The authors thank Bharath Bannur and Sunil Walia for the conductivity measurements.

References

1. Novoselov, K. S.; Geim, A. K.; Morozov, S. V.; Jiang, D.; Zhang, Y.; Dubonos, S. V.; Grigorieva, I. V.; Firsov, A. A. *Science* **2004,** *306,* 666–669. doi:10.1126/science.1102896
2. Novoselov, K. S.; Jiang, D.; Schedin, F.; Booth, T. J.; Khotkevich, V. V.; Morozov, S. V.; Geim, A. K. *Proc. Natl. Acad. Sci. U. S. A.* **2005,** *102,* 10451–10453. doi:10.1073/pnas.0502848102
3. Kumar, P. V.; Bardhan, N. M.; Tongay, S.; Wu, J.; Belcher, A. M.; Grossman, J. C. *Nat. Chem.* **2014,** *6,* 151–158. doi:10.1038/nchem.1820
4. Rao, C. N. R.; Sood, A. K.; Subrahmanyam, K. S.; Govindaraj, A. *Angew. Chem., Int. Ed.* **2009,** *48,* 7752–7777. doi:10.1002/anie.200901678
5. Rao, C. N. R.; Matte, H. S. S. R.; Subrahmanyam, K. S. *Acc. Chem. Res.* **2013,** *46,* 149–159. doi:10.1021/ar300033m
6. Zhu, X.; Zhu, Y.; Murali, S.; Stoller, M. D.; Ruoff, R. S. *ACS Nano* **2011,** *5,* 3333–3338. doi:10.1021/nn200493r
7. Kholmanov, I. N.; Domingues, S. H.; Chou, H.; Wang, X.; Tan, C.; Kim, J.-Y.; Li, H.; Piner, R.; Zarbin, A. J. G.; Ruoff, R. S. *ACS Nano* **2013,** *7,* 1811–1816. doi:10.1021/nn3060175
8. Abid; Sehrawat, P.; Islam, S. S.; Mishra, P.; Ahmad, S. *Sci. Rep.* **2018,** *8,* 3537. doi:10.1038/s41598-018-21686-2
9. Hummers, W. S., Jr.; Offeman, R. E. *J. Am. Chem. Soc.* **1958,** *80,* 1339. doi:10.1021/ja01539a017
10. Hossain, M. Z.; Johns, J. E.; Bevan, K. H.; Karmel, H. J.; Liang, Y. T.; Yoshimoto, S.; Mukai, K.; Koitaya, T.; Yoshinobu, J.; Kawai, M.; Lear, A. M.; Kesmodel, L. L.; Tait, S. L.; Hersam, M. C. *Nat. Chem.* **2012,** *4,* 305–309. doi:10.1038/nchem.1269
11. Kim, K. S.; Zhao, Y.; Jang, H.; Lee, S. Y.; Kim, J. M.; Kim, K. S.; Ahn, J.-H.; Kim, P.; Choi, J.-Y.; Hong, B. H. *Nature* **2009,** *457,* 706–710. doi:10.1038/nature07719
12. Subrahmanyam, K. S.; Vivekchand, S. R. C.; Govindaraj, A.; Rao, C. N. R. *J. Mater. Chem.* **2008,** *18,* 1517–1523. doi:10.1039/b716536f

13. Li, X.; Cai, W.; An, J.; Kim, S.; Nah, J.; Yang, D.; Piner, R.; Velamakanni, A.; Jung, I.; Tutuc, E.; Banerjee, S. K.; Colombo, L.; Ruoff, R. S. *Science* **2009,** *324,* 1312–1314. doi:10.1126/science.1171245
14. Subrahmanyam, K. S.; Panchakarla, L. S.; Govindaraj, A.; Rao, C. N. R. *J. Phys. Chem. C* **2009,** *113,* 4257–4259. doi:10.1021/jp900791y
15. Campos-Delgado, J.; Romo-Herrera, J. M.; Jia, X.; Cullen, D. A.; Muramatsu, H.; Kim, Y. A.; Hayashi, T.; Ren, Z.; Smith, D. J.; Okuno, Y.; Ohba, T.; Kanoh, H.; Kaneko, K.; Endo, M.; Terrones, H.; Dresselhaus, M. S.; Terrones, M. *Nano Lett.* **2008,** *8,* 2773–2778. doi:10.1021/nl801316d
16. Choucair, M.; Thordarson, P.; Stride, J. A. *Nat. Nanotechnol.* **2009,** *4,* 30–33. doi:10.1038/nnano.2008.365
17. Huang, H.-H.; De Silva, K. K. H.; Kumara, G. R. A.; Yoshimura, M. *Sci. Rep.* **2018,** *8,* 6849. doi:10.1038/s41598-018-25194-1
18. Sokolov, D. A.; Shepperd, K. R.; Orlando, T. M. *J. Phys. Chem. Lett.* **2010,** *1,* 2633–2636. doi:10.1021/jz100790y
19. Kumar, P.; Subrahmanyam, K. S.; Rao, C. N. R. *Int. J. Nanosci.* **2011,** *10,* 559–566. doi:10.1142/s0219581x11008824
20. Gilje, S.; Dubin, S.; Badakhshan, A.; Farrar, J.; Danczyk, S. A.; Kaner, R. B. *Adv. Mater. (Weinheim, Ger.)* **2010,** *22,* 419–423. doi:10.1002/adma.200901902
21. Park, S.; An, J.; Jung, I.; Piner, R. D.; An, S. J.; Li, X.; Velamakanni, A.; Ruoff, R. S. *Nano Lett.* **2009,** *9,* 1593–1597. doi:10.1021/nl803798y
22. Shin, H.-J.; Kim, K. K.; Benayad, A.; Yoon, S.-M.; Park, H. K.; Jung, I.-S.; Jin, M. H.; Jeong, H.-K.; Kim, J. M.; Choi, J.-Y.; Lee, Y. H. *Adv. Funct. Mater.* **2009,** *19,* 1987–1992. doi:10.1002/adfm.200900167
23. Wang, G.; Yang, J.; Park, J.; Gou, X.; Wang, B.; Liu, H.; Yao, J. *J. Phys. Chem. C* **2008,** *112,* 8192–8195. doi:10.1021/jp710931h
24. Zhu, C.; Guo, S.; Fang, Y.; Dong, S. *ACS Nano* **2010,** *4,* 2429–2437. doi:10.1021/nn1002387
25. Park, O.-K.; Choi, Y.-M.; Hwang, J. Y.; Yang, C.-M.; Kim, T.-W.; You, N.-H.; Koo, H. Y.; Lee, J. H.; Ku, B.-C.; Goh, M. *Nanotechnology* **2013,** *24,* 185604. doi:10.1088/0957-4484/24/18/185604
26. Porwal, J.; Karanwal, N.; Kaul, S.; Jain, S. L. *New J. Chem.* **2016,** *40,* 1547–1553. doi:10.1039/c5nj02095f
27. Purkait, T.; Singh, G.; Kumar, D.; Singh, M.; Dey, R. S. *Sci. Rep.* **2018,** *8,* 640. doi:10.1038/s41598-017-18593-3
28. Down, M. P.; Rowley-Neale, S. J.; Smith, G. C.; Banks, C. E. *ACS Appl. Energy Mater.* **2018,** *1,* 707–714. doi:10.1021/acsaem.7b00164
29. Cao, J.; He, P.; Brent, J. R.; Yilmaz, H.; Lewis, D. J.; Kinloch, I. A.; Derby, B. *ACS Appl. Mater. Interfaces* **2018,** *10,* 10330–10338. doi:10.1021/acsami.7b18853

License and Terms

The definitive version of this article is the electronic one which can be found at:
doi:10.3762/bjnano.11.7

BEILSTEIN JOURNAL OF NANOTECHNOLOGY

Electrochemically derived functionalized graphene for bulk production of hydrogen peroxide

Munaiah Yeddala‡, Pallavi Thakur‡, Anugraha A and Tharangattu N. Narayanan*

Full Research Paper

Address:
Tata Institute of Fundamental Research - Hyderabad, Sy. No. 36/P,
Gopanapally Village, Serilingampally Mandal, Hyderabad 500107,
India

Email:
Tharangattu N. Narayanan* - tnn@tifrh.res.in

* Corresponding author ‡ Equal contributors

Keywords:
electrochemical oxygen reduction; functionalized carbon; functionalized graphene; H_2O_2 production; water treatment

Beilstein J. Nanotechnol. **2020,** *11,* 432–442.
doi:10.3762/bjnano.11.34

Received: 28 October 2019
Accepted: 13 February 2020
Published: 09 March 2020

This article is part of the thematic issue "Graphene and beyond".

Guest Editor: G. U. Kulkarni

Abstract

On-site peroxide generation via electrochemical reduction is gaining tremendous attention due to its importance in many fields, including water treatment technologies. Oxidized graphitic carbon-based materials have been recently proposed as an alternative to metal-based catalysts in the electrochemical oxygen reduction reaction (ORR), and in this work we unravel the role of C=O groups in graphene towards sustainable peroxide formation. We demonstrate a versatile single-step electrochemical exfoliation of graphite to graphene with a controllable degree of oxygen functionalities and thickness, leading to the formation of large quantities of functionalized graphene with tunable rate parameters, such as the rate constant and exchange current density. Higher oxygen-containing exfoliated graphene is known to undergo a two-electron reduction path in ORR having an efficiency of about 80 ± 2% even at high overpotential. Bulk production of H_2O_2 via electrolysis was also demonstrated at low potential (0.358 mV vs RHE), yielding ≈34 mg/L peroxide with highly functionalized (≈23 atom %) graphene and ≈16 g/L with low functionalized (≈13 atom %) graphene, which is on par with the peroxide production using state-of-the-art precious-metal-based catalysts. Hence this method opens a new scheme for the single-step large-scale production of functionalized carbon-based catalysts (yield ≈45% by weight) that have varying functionalities and can deliver peroxide via the electrochemical ORR process.

Introduction

Hydrogen peroxide (H_2O_2) is identified as one among the most important 100 chemicals in the world, and its applications extend from the pharmaceutical industry to water purification [1-3]. Today, a majority of the required H_2O_2 is produced through the complex and energy-intensive anthraquinone method [4], and although it is popular, it has drawbacks such as side reactions, which consume the catalyst leading to the regeneration and hydrogenation of the catalyst [4]. Alternative routes for peroxide generation include direct preparation of H_2O_2 from oxygen and hydrogen, oxidation of alcohols [5], photocatalysis [6], and electrochemical processes such as the electro-Fenton process [7], microbial electrosynthesis [8], and proton exchange membrane (PEM) assisted synthesis [9]. Further, in situ generation of peroxide from dissolved oxygen via electrochemical ORR is identified as an effective route for water treatment technology, where economically viable, biologically friendly, sustainable catalysts are required [10-14].

Of the various routes, the direct synthesis of H_2O_2 through the reaction between H_2 and O_2 in the presence of a catalyst [15] is one of the possible routes having high yield, while the direct mixing of H_2 and O_2 can be explosive in nature [16], and hence requires a large quantity of another gas such as N_2 and CO_2 to dilute the reactant gases [17]. Electrochemical synthesis methods such as the PEM fuel cell reactor-based method can overcome this limitation; however, this method relies on expensive membranes to separate hydrogen and oxygen and to directly yield H_2O_2 from them [18]. Later, this method was modified by generating protons (H^+) through water oxidation which eliminated the direct purging of H_2 gas [9]. The major roadblock in this method is the development of a sustainable electrocatalyst for the selective reduction of oxygen to H_2O_2 [19-23]. Today, most electrochemical H_2O_2 production methods rely on precious-metal-based materials or transition metal and/or metal oxides, and hence their economic viability for the future technologies is highly questionable [10,24-27]. Hence new metal-free electrode materials for H_2O_2 generation are highly sought after for future technologies.

Recently, carbon-based catalysts have emerged as an alternate material for existing metal-based technologies [28,29]. For example, carbon nanotubes (CNTs) have been well studied for their catalytic activity, although conflicting reports exist due to the presence of unavoidable metallic impurities present [30-33]. With the emergence of graphene, heteroatom doping in sp^2 graphitic structures is found to be an engineering pathway for altering the inert catalytic activity of planar honeycomb lattices of graphene and its derivatives [34,35]. It has been found that certain heteroatoms doped into graphene can even outperform the benchmark catalysts such as platinum (Pt/C) in their long-run alkaline ORR process where the extended stability in electrochemical processes is one of the crucial issues with Pt/C [36]. In all of these doped systems, carbon atoms near to the defect centers are found as catalytically active centers [37]. Recently, an ultra-small amount of selenium (Se) edge functionalized graphene (reduced graphene oxide (rGO)) was found to undergo a direct four-electron path ORR process in alkaline medium, where rGO undergoes a two-electron path peroxide route ORR [35]. In this process, Se acts as a single atom site catalyst. In a nutshell, depending on the nature of the dopant and its position in the host lattice, it has been well reported that one can engineer the electrochemical activity of nanographitic systems and the catalytic reaction pathways [31,38-40].

Very recently, oxidized graphitic structures were identified for their efficacy towards the alkaline ORR process leading to selective peroxide production. In a recently reported theoretical study by Cui et al., the carbon atoms near the oxygen functionalities are used for their ORR efficacy via a two-electron pathway [37]. It was further experimentally shown that carbon materials such as CNTs, graphene, etc. can be oxidized via chemical treatment, and these oxidized forms of sp^2–sp^3 carbon systems prefer peroxide formation in alkaline ORR process [25]. Such studies are supported by reports from other groups, where McCloskey et al. showed that sp^2-hybridized carbon near-ring ether defects along sheet edges are the most active sites for peroxide production in rGO [3]. They also showed that the performance of these rGO-based catalysts in alkaline conditions under low overpotential outperform the existing state-of-the-art catalysts. However, a large extent of oxidation may hamper the charge transfer properties of functionalized graphene (graphene oxide (GO) or other functional derivatives of graphene) [41]. Hence the single-step method for the production of large scale, controllably functionalized graphene is of high demand, and in this work, we demonstrate such a method to control the extent of oxidation. Further, although it was proposed that C=O (quinone) functional groups are the major candidates in deciding the peroxide route O_2 reduction, here we provide experimental evidence for tuning the quinone groups in graphene and its correlation to the peroxide production.

In one of our previous works, different halogenated graphene materials were developed via a single-step electrochemical exfoliation (EE) method [42]. It was found that such a method can produce graphene with varying degrees of oxygen functionalities [43]. Here we explore the possibility of functional groups to control graphene toward the electrochemical production of H_2O_2 in alkaline medium, and the amount of peroxide generated is quantified using a spectroscopic technique. A large amount of H_2O_2 is found to be formed via such simple modification of the exfoliation parameters, and the details are discussed in this article.

Results and Discussion

The detailed physical characterization of electrochemically exfoliated graphene (EEG) was given in our recent report, where the variation in the oxygen functionalities, amount of fluorine content in exfoliated graphene, etc. were shown [43]. As discussed previously, the surface oxygen functional groups are crucial for the reduction of molecular oxygen to H_2O_2 and hence high-resolution O 1s X-ray photoelectron spectroscopy (XPS) was carried out. The O 1s peaks of different EEG samples are shown in Figure 1a. It can be seen that the intensity of the O 1s peak decreases from G-M1 to G-M4 (where G refers to graphene and M1, M2, M3, and M4 refer to the respective

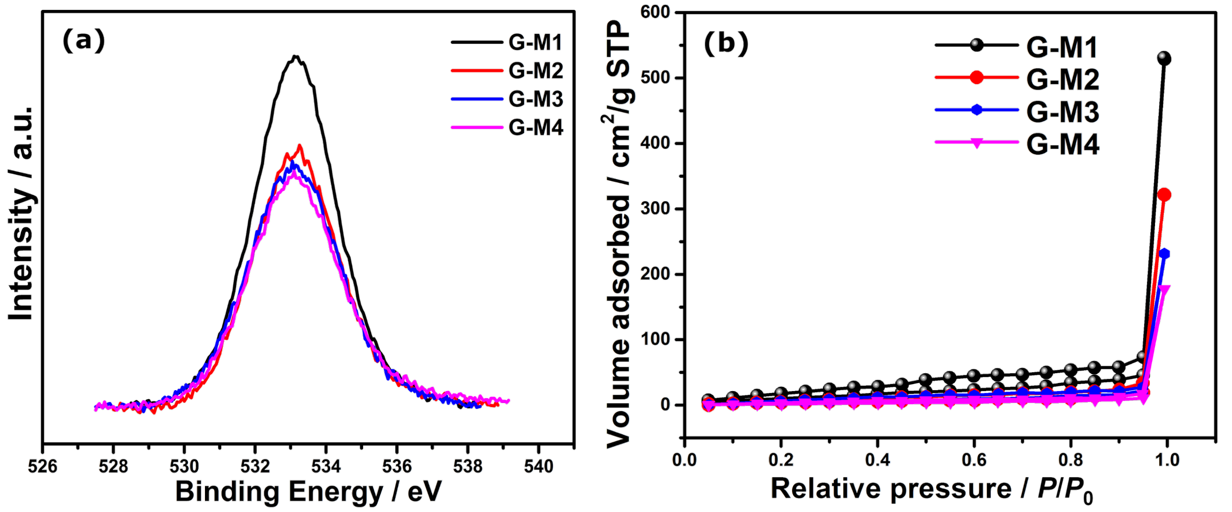

Figure 1: (a) High resolution O 1s XPS spectra of different EEG samples. (b) BET isotherms of different EEG samples.

molarity of the electrolyte used for the exfoliation), and the elemental composition calculated from the survey spectrum of the materials revealed that the degree of oxygen functionalization varies from ≈21 to ≈10 atom % from G-M1 to G-M4 (as inferred from the XPS survey spectrum as well as the high-resolution C 1s and O 1s XPS spectra (Supporting Information File 1, Figure S1a)) [43]. The O 1s spectrum can be deconvoluted into two distinct peaks (as shown in Figure S2) centered at 532.2 eV and 533.4 eV, corresponding to alcoholic (C–OH)/ ether type of oxygen in ester functional groups and carbonyl (C=O in –COOH) functional groups, respectively [42,44]. Interestingly, irrespective of the degree of functionalization (oxygen content), carbonyl groups are found to be the major component in all the EEG samples. This correlates with the Fourier-transform infrared spectroscopy (FTIR) based analysis (Figure S1b), which also shows the presence of covalent C–F functional groups in all the samples. The samples also contain fluorine as one of the dopants with a content varying from 2.3 to 3.9 atom %. However, previous studies showed that the fluorine-doped graphene systems follow a direct four-electron ORR path [45-48], whereas some of the other fluorine-doped carbon prefers the H_2O_2 path during the ORR [49,50]. Along with the degree of functionalization, the surface area of the material can also influence the catalytic property of the materials since these EEG samples are derived from bulk graphite using a single-step exfoliation in different electrolytes. The BET isotherms of the EEG samples are shown in Figure 1b. The shape of the nitrogen adsorption and desorption curves displays a typical type III behavior, which corresponds to that of a layered material [42,51]. The surface area varies from 46 ± 2 m^2/g (G-M1) to 11 ± 2 m^2/g (G-M4). The change in the surface area can be attributed to the rate of exfoliation of the graphite rod which in turn depends upon the availability of fluoride and hydroxide ions at the anode (i.e., the higher the hydroxide ions the faster the exfoliation), which is in line with our recent report [43].

As described earlier, transmission electron microscopy (TEM) images of EEG samples indicate that the average lateral size is about 3–5 µm (more images in Supporting Information File 1) and scanning electron microscopy (SEM) images indicate the formation of randomly oriented exfoliated graphene nanosheets [43]. However, the TEM images show that the thickness of the graphene increases from G-M1 to G-M4, where the G-M4 is found to block the electron beam despite its layered nature (Supporting Information File 1, Figure S2). Here the thickness variation is confirmed using atomic force microscopy (AFM), and the results are given in Figure S3. This indicates that with an increase in the concentration of the electrolyte, the thickness is increased from 40 nm to 140 nm (Figure S3), which corresponds with the TEM analysis [43] and BET-based surface area data. Hence from the TEM, BET, and AFM analysis, it can be concluded that the electrolyte concentration is important for the electrochemical exfoliation assisted synthesis of ultrathin graphene layers, and the electrolyte concentration also determines the extent of functionalization of graphene.

The presence of the C=O groups is further confirmed by cyclic voltammetry (CV) measurements in alkaline and acidic electrolyte. The CV profiles of the EEG samples (EEG-modified glassy carbon electrode (GCE) as the working electrode in a three-electrode set up) in the acidic and alkaline medium between −0.2 to 1.2 V vs RHE at 100 mV/s scan rate are shown in Figure 2. Two distinct features observed in the CV profiles are: the difference in the area under the curve of the different EEG samples, which indicates the difference in the surface area of the electrodes; and secondly, the Faradaic redox peaks in acidic

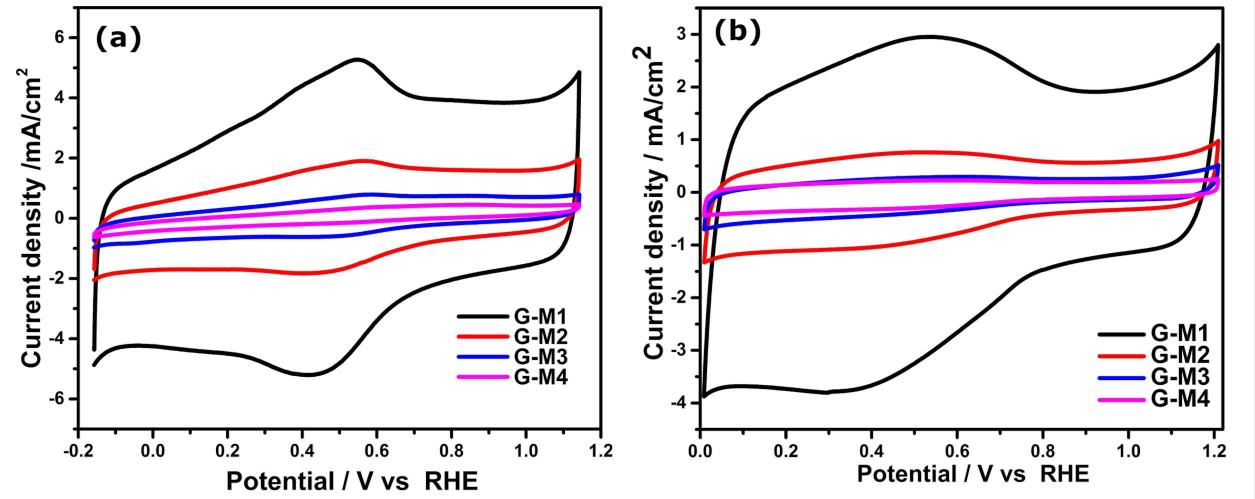

Figure 2: The CV profiles of different EEG samples in (a) acidic (0.5 M H_2SO_4) and (b) alkaline (0.1 M KOH) electrolyte at 100 mV/s scan rate. The CV with low scan rate (5 mV/s) is shown in Supporting Information File 1, Figure S4a. The current densities are calculated using the geometrical area.

CV curves, which is nearly absent under alkaline conditions. Under both conditions (alkaline and acidic), G-M1 shows the highest surface area and G-M4 showed the lowest. This systematic variation in the electrochemical surface area corresponds with the BET analysis.

As mentioned, the CV profiles in the acidic medium show redox peaks at ≈0.5 V (0.5 M H_2SO_4), which corresponds to the redox reaction of oxygen functional groups such as quinone to hydroquinone, as per the following equation [52-54]:

$$Q + 2H^+ \leftrightarrow QH_2 \qquad (1)$$

Interestingly, the intensity of the peak increases with the degree of functionalization, which further supports the assumption that the redox peak at 0.5 V is due to functionalization. These results are in good agreement with XPS data, as discussed previously. These redox peaks are not observed (only broad peaks) in alkaline medium (Figure 2b) under identical conditions due to the lack of the supply of protons (in acidic media, the conversion is $2H^+$, $2e^-$ reduction while in alkaline media it is only $2e^-$ reduction where Q^{2-} stabilized by water molecules and all species Q^{2-}, QH^-, QH^{2-} are present in equilibrium). This indicates the presence of C=O groups and their role in electrochemical processes.

The ORR activity of different EEG samples is estimated using a conventional three-electrode system. The CV profiles of EEG-modified GCE in 0.1 M KOH electrolyte saturated with N_2 and O_2 gas are displayed in Figure 3. The electrodes exhibit capacitive (double layer) behavior in N_2-saturated electrolyte, while a sharp reduction peak corresponding to oxygen reduction in O_2-saturated electrolyte is shown in all the cases. The intensity of the peak (peak current density) corresponds to the ORR process and varies with the degree of oxygen functionalities (from G-M1 to G-M4), which reveals the effect of the degree of functionalization in ORR. The CV profiles plotted using the current densities calculated using the electrochemical surface area also shown similar trends, as shown in Supporting Information File 1, Figure S5 (the detailed procedure to calculate electrochemical surface area is given in the Supporting Information File 1, see Figure S6). To summarize, the G-M1 sample showed the highest reduction current under the same experimental conditions whereas G-M4 showed the lowest current with the rest of the samples in between these two samples.

To understand the ORR reaction pathway, rotating ring and disk electrode (RRDE)-based hydrodynamic voltammetry is conducted. Figure 4a shows ORR linear sweep voltammetry (LSV) scans of different EEG samples on GCE disk (4 mm diameter) and the H_2O_2 oxidation over the platinum ring (potential kept at 1.5 V vs RHE) at 10 mV/s scan rate at 1600 rotation per minute (rpm) for the electrode. The experiments are also carried out at different rotation speeds, and the data is given in Supporting Information File 1, Figure S7. The electrochemical parameters derived from these experiments (at 0.358 V vs RHE) are shown in Table 1. As shown in the Figure 4, the current density and onset potential of the reaction vary with the degree of (oxygen) functionalization. A benchmark Pt/C catalyst performance is also shown for comparison.

The onset potential of ORR is found to become more favorable with a high degree of functionalization, reaching 860 mV for the G-M1 electrode and 770 mV for the G-M4 sample. The onset potential and current density of G-M2 and G-M3 are

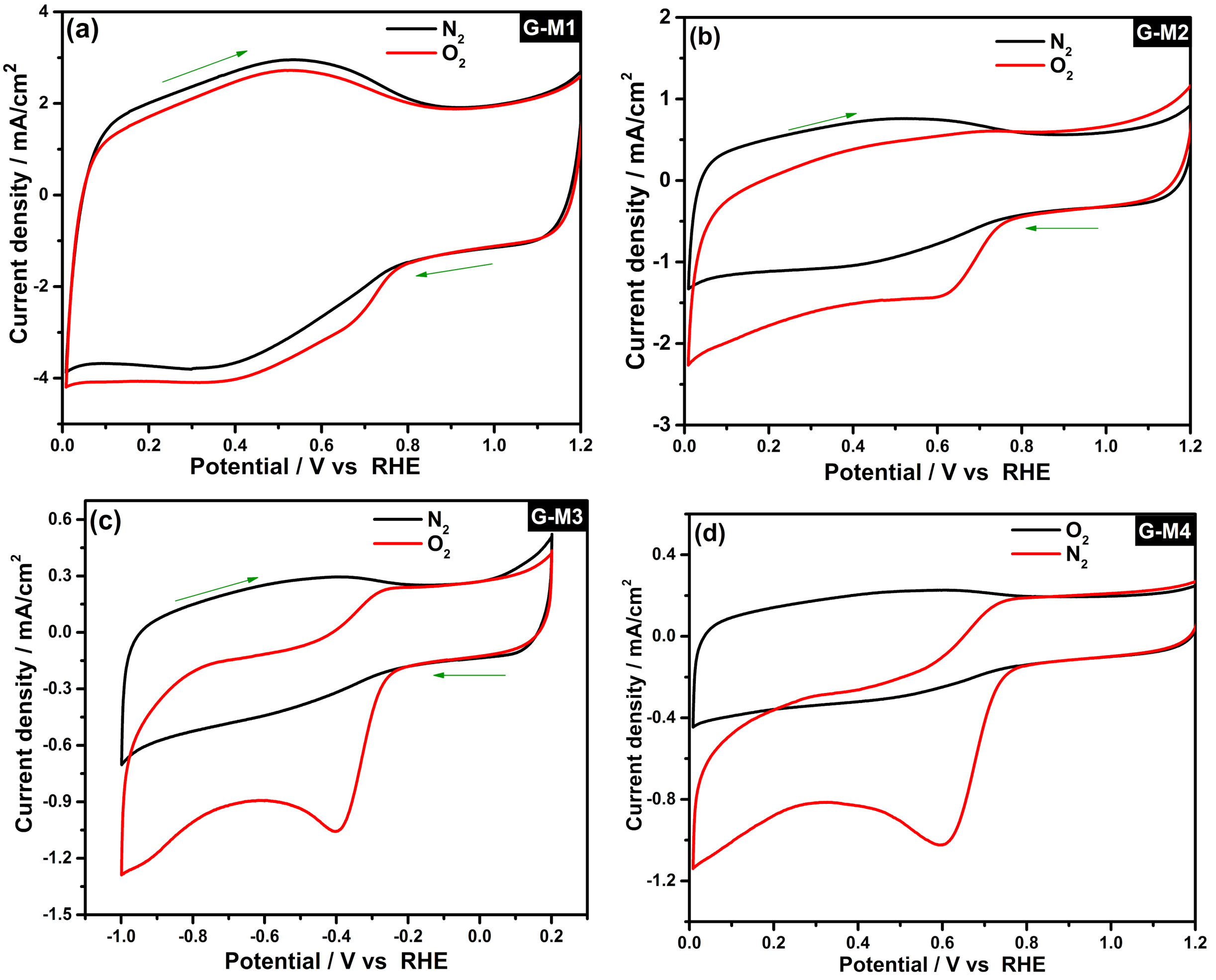

Figure 3: The CV profiles of different electrodes in 0.1 M KOH electrolyte saturated with N_2 and O_2. The current density is calculated using the geometrical surface area.

found to be between those of G-M1 and G-M4. Interestingly, the difference in fluorine content (which is nominal) did not affect the onset potential of the ring current. The shape of the LSV scans shows a two-step in reduction, which is due to the reduction of oxygen to H_2O_2 at lower overpotential and its further reduction to H_2O at higher potentials [44]. This suggests that the ORR proceeds through a two-electron reduction path in EEG samples while the sharp Faradaic current enhancement followed by a plateau in Pt/C shows that it is a one-step reduction process.

The quantity of H_2O_2 produced is analyzed using a platinum ring electrode at 1.5 V vs RHE. The ring current is higher (0.067 mA) for highly functionalized graphene and less (0.028 mA) for less functionalized (G-M4) graphene, which displays higher peroxide formation in G-M1. Hence G-M1 shows higher O_2 reduction current and higher peroxide oxidation than the others because the oxygen functionalities possess selective activity towards ORR, which is in line with the other recent reports [37]. The number of electrons transferred per oxygen molecule and percentage (%) of H_2O_2 produced during ORR are calculated (using the details given in Supporting Information File 1), and the data are shown in Figure 4b and 4c, respectively.

Table 1 gives the kinetic parameters calculated from Figure 4a (LSV of ORR on RRDE) at 0.358 V vs RHE. As shown in the table, all the EEG samples, irrespective the degree of functionalization, show the number of electrons transferred as ≈2.4 electrons per oxygen and yield ≈80 ± 2% H_2O_2 generation. Figure 4c shows the number of electrons transferred over a potential range from 0.608 to 0.108 V vs RHE. Interestingly, the ORR follows the peroxide reduction path (about 2.2 ± 0.1 electron per oxygen molecule at 0.4V vs RHE) at lower overvoltage, and the slight increase can be observed in the number of electrons transferred at higher overpotential. The

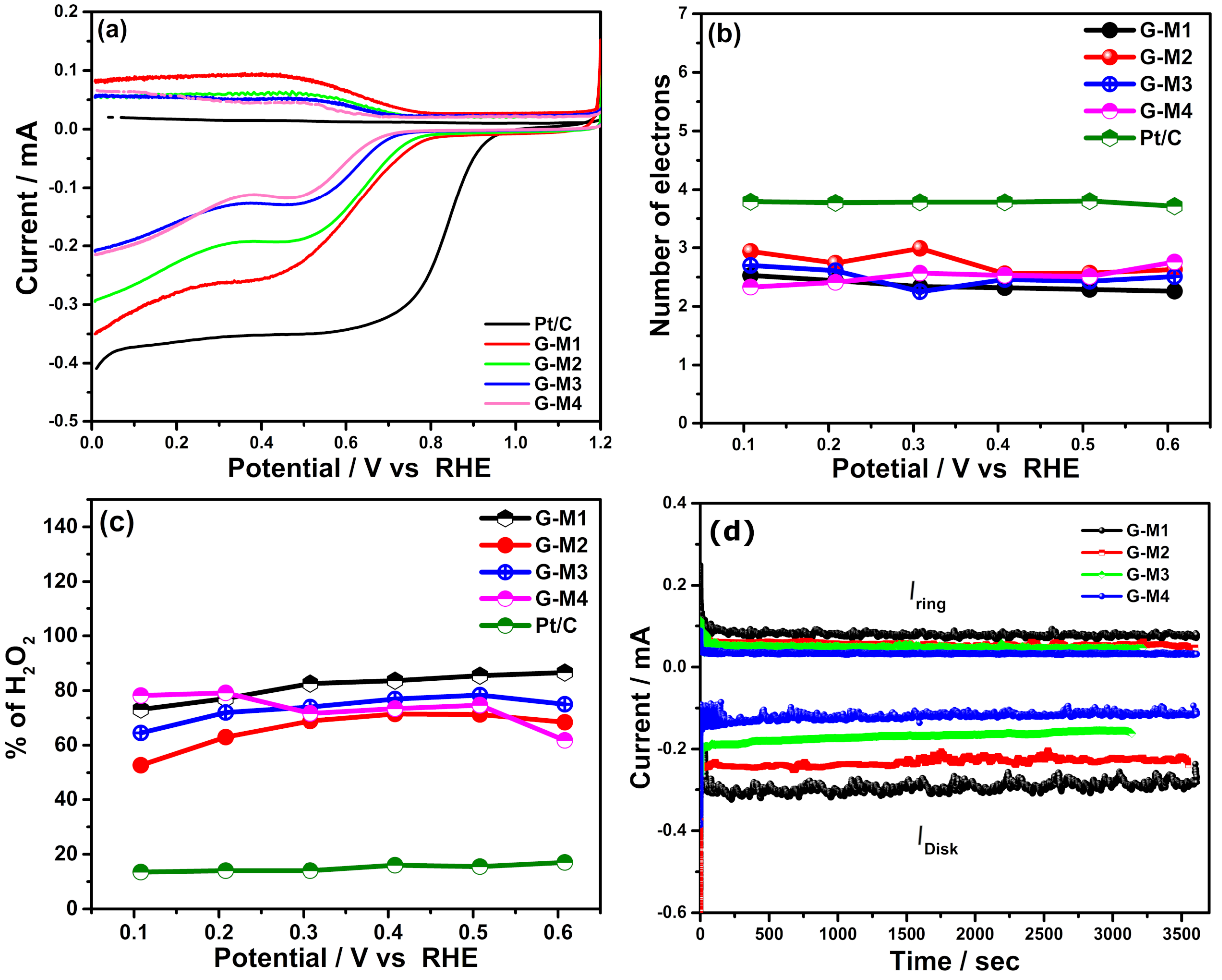

Figure 4: (a) LSV scans of O_2 reduction and H_2O_2 (HO_2^-) oxidation on different EEG-modified RRDE samples. (b) The number of electrons transferred during ORR per O_2 molecule and (c) the percentage (%) of formed H_2O_2 (calculated from Figure 4a) is shown. (d) Chronoamperograms of O_2 reduction and H_2O_2 oxidation processes at 0.358 V and 1.5 V vs RHE on different electrodes.

Table 1: The RRDE experiment electrochemical parameters obtained at 0.358 V (vs RHE, from Figure 4a).

Active materials	Disk current (mA)	Ring current (mA)	Onset potential (V)	Number of electrons (*n*)	% H_2O_2 at 0.358 V
G-M1	0.24	0.067	0.86	2.35	82.07
G-M2	0.18	0.046	0.84	2.41	79.09
G-M3	0.12	0.031	0.81	2.43	78.43
G-M4	0.11	0.028	0.77	2.40	80.01
Pt/C	0.32	0.015	1.01	3.65	17

increase in the number of electrons can be attributed to fluorine functional groups attached to graphene, which can undergo a direct 4-electron path at higher overpotential, as reported previously [47,55]. Highly fluorinated EEG (G-M2) shows about three electrons per oxygen at higher overpotential (0.3008 to 0.108 V). However, it is found that the fluorine content can be reduced by reducing the concentration of the electrolyte, which further improves the selective production of H_2O_2 even at relatively higher overpotential.

In order to test the stability of these catalysts, chronoamperometry experiments were conducted using RRD electrodes where the disk current was kept at 0.358V vs RHE and the ring potential was kept at 1.5 V vs RHE. Figure 4d depicts the chronoamperograms of the ORR at the disk and H_2O_2 oxidation at the ring electrode for 1 h at 1600 rpm, which shows reasonable stability in the current over time (both electrodes). Furthermore, the variation in the current at the ring and disk for different EEG samples follows the same trend as that found in the LSV scans (Figure 4a). The stability of the EEG-based catalysts is also tested by repeated cycling of LSV at 1600 rpm for 1000 cycles (at 100 mV·s^{-1}). The LSV scans of ORR before and after 1000 cycles are given in Supporting Information File 1, Figure S8 and the results show that all the EEG samples, irrespective of the degree of functionalization, display very little degradation in performance. This indicates that the functionalized EEG samples are stable electrocatalysts for electrochemical H_2O_2 production even under harsh alkaline conditions.

Hence it can be concluded that the presence of oxygen functional groups is a key factor in improving the ORR, and they undergo the redox process during the reaction in acidic medium (see Figure 2a). In order to test the durability of the materials in acidic medium, chronoamperometry studies were carried out in 0.5 M H_2SO_4 at 0.45 V vs RHE for 3 h. The EEG samples were studied (before and after chronoamperometry) using Raman and FTIR spectroscopy along with the electrochemical performance in 0.1 M KOH solution, and the data is given in Figure 5. In Figure 5a, the Raman spectra of EEG before and after 3 h of chronoamperometry are shown, which show no appreciable change in either the peak position or peak intensity. This indicates that no additional defects are created during the experiment. The important Raman peaks are marked in the figure and the shoulder peak in "G" is due to the additional single phonon intra-valley scattering process (named as D') which is due to the presence of defects. However, the FTIR spectrum (see Figure S4b) shows evidence for the formation of OH functional groups during the chronoamperometry, which is suggests that most of the C=O functional groups are converted into –C–OH during the reaction. To study the effect of the change in the functionalization on ORR, we recorded the CV of ORR in 0.1 M KOH solution before and after chronoamperometry. Such changes are found to have an insignificant effect on the performance of the material towards ORR (see Figure 5b).

To evaluate the EEG samples further, the kinetic parameters such as rate constant and exchange current density are calculated from the Tafel plot analysis (in O_2-saturated electrolyte) and are shown in Figure 6. As expected, G-M1 shows a high exchange current 1.2 × 10^{-5} A, and G-M4 shows a low exchange current 7.4 × 10^{-6} A, which demonstrates that G-M1 is kinetically more favorable towards ORR than G-M4. The rate constant (k) was calculated from the following equation [56], which is derived from the Butler–Volmer model [56]:

$$i_o = FAk^0 C_O^{*(1-\alpha)} C_R^{*\alpha} \qquad (2)$$

where i_o is the exchange current density, F is the Faraday constant (96485 C), C_O^* is the concentration of the oxidant, C_R^* is the concentration of the reductant, α is the transfer coefficient, A is the surface area of the electrode (0.07 cm^2), and k^0 is the

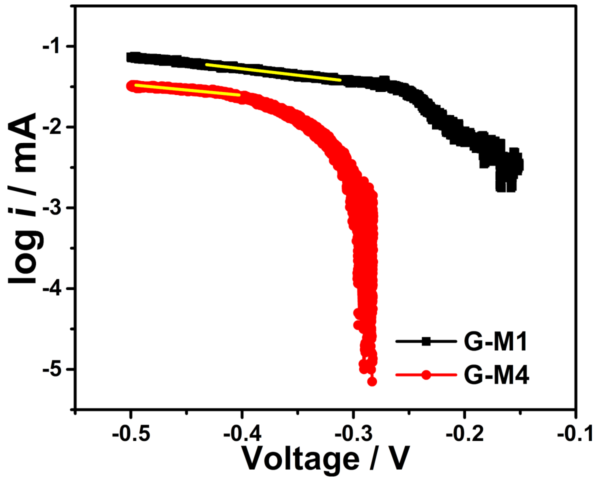

Figure 6: Tafel plots of ORR over EEG-modified electrodes in 0.1 M KOH O_2-saturated electrolyte.

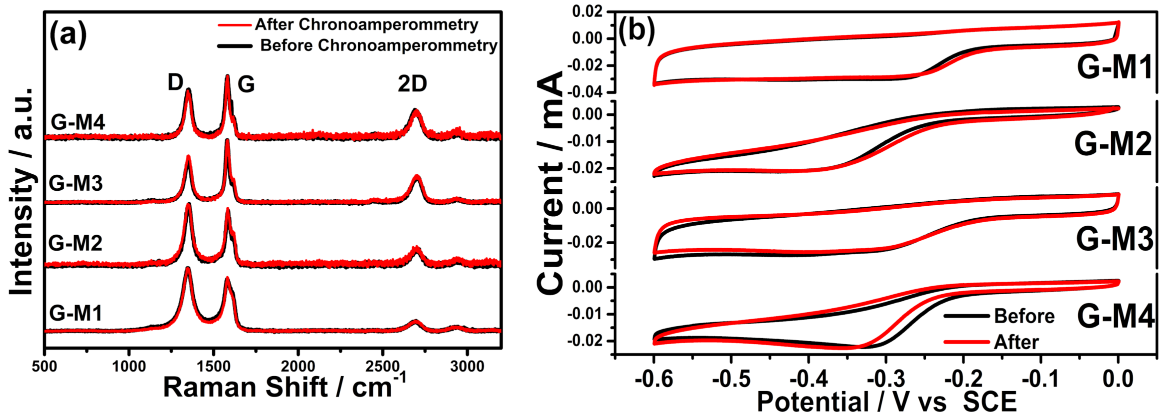

Figure 5: (a) Raman spectra of EEG samples before and after 3 h of chronoamperometry in 0.5 M H_2SO_4 solution at 0.45 V vs RHE. (b) ORR in 0.1 M KOH solution before and after chronoamperometry.

heterogeneous rate constant. In this case, we considered $C_O = C_R = C$, where C is the concentration of the dissolved oxygen which is 1.26×10^{-6} mol·cm^{-3} [57,58]. The rate constant value calculated from the above equation is 1.39×10^{-3} cm·s^{-1} for G-M1 and 8.52×10^{-4} cm·s^{-1} for G-M4 which follow the trend observed in exchange current density. Both i_o and k^0 emphasize the importance of the quantity of functional groups in ORR.

Large-scale production of peroxide using these EEG samples are conducted using bulk electrolysis. EEG-coated and uncoated graphite paper was employed for the electrochemical production of H_2O_2. The H_2O_2 produced through ORR is also quantified using a $Ce(SO_4)_2$ solution assisted UV–visible absorbance based analysis, where the details and calibration are given in Supporting Information File 1. Figure 7a shows chronoamperograms of ORR on EEG-coated graphite papers at 0.358 V vs RHE in 0.1 M KOH electrolyte for 3 h. G-M1 shows the highest current where the current subsequently reduced from sample G-M1 to G-M4. The amount of H_2O_2 produced is calculated as 34.5, 31.6, 23.4, and 16.4 mg/L for G-M1, G-M2, G-M3, and G-M4, respectively. The high quantity of H_2O_2 production in G-M1 can be attributed to its high degree of oxygen functional groups, particularly due to C=O. The amount of peroxide formed by this method is found to be higher or on par with recent reports [3]. This opens an efficient pathway for the single-step large-scale production of peroxide-generating carbon-based ORR catalysts.

The weight of the anode (graphite electrode) used for the electrochemical exfoliation was ≈0.374 g and the 1–2 h of exfoliation resulted in the complete consumption of graphite, delivering ≈0.180 ± 0.005 g of exfoliated functionalized graphene. Hence the average yield of this process was found to be ≈45%.

Hence such chemically modified graphene powders, which are proven to be dispersible in a variety of organic solvents [59], offer alternate possibilities towards existing metal-based peroxide generation technologies. Controlling the electronic properties via the thermal reduction method can further tune the charge transfer properties of such functionalized graphene powders [60], opening a plethora of opportunities in this field.

Conclusion

An efficient single-step method (without any post-treatment) has been developed for the high-yield synthesis of carbon-based peroxide, generating ORR catalysts having varying functionalities. The role of quinone-containing functional groups in graphene towards the electrochemical ORR process is unraveled, and the higher C=O content results in a large amount of H_2O_2 production at a high rate. The other functionalities in graphene such as fluorine have a minimal role in lower potential reduction reactions while they become prominent at higher potentials, where they undergo a direct four-electron reduction of O_2 to water. The concentration of the electrolyte was found to be related to the thickness of the formed exfoliated graphene and its functionalities, and the 1 M KF-based exfoliation resulted in ultrathin layers for the sample G-M1, which had a high amount of C=O groups but fewer C–F functionalities. These electrochemically exfoliated functionalized graphene samples are found to be highly stable in alkaline electrochemical conditions, whereby 3 h of ORR produced ≈34 mg/L of peroxide for an applied potential of 0.358 V vs RHE, indicating

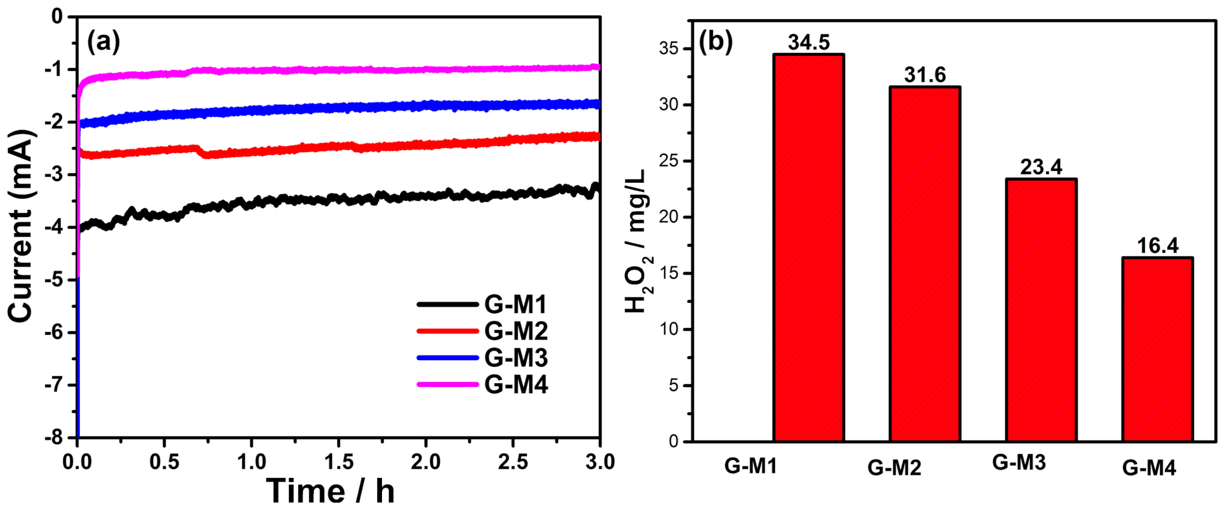

Figure 7: (a) Chronoamperogram of O_2 reduction at 0.358 V on graphite paper modified with EEG. (b) The amount of H_2O_2 produced by each sample is shown in Figure 7b.

a production on par or higher than the recently reported state-of-the-art catalysts [3].

Experimental

Materials

Graphite rods of 3 mm diameter and 150 mm length with 99.999% purity, sodium hydroxide (ACS grade), sulfuric acid, and hydrogen peroxide (27% w/v) were obtained from Alfa Aesar. Nafion solution (5% w/w) was purchased from Sigma-Aldrich, and potassium fluoride (KF) and $Ce(SO_4)_2$ were obtained from Sisco research laboratories, India. All of the high purity chemicals were employed as-received without any further purification. Ultrahigh purity oxygen (99.999%) was used for electrochemical reactions.

Synthesis of electrochemically exfoliated graphene (EEG)

EEG was synthesized via a method reported previously [42,43], where the degree of functionalization can be tuned by changing the concentration of the electrolyte (KF) from 1 to 4 M. In this process, two graphite rods were used as electrodes in KF aqueous electrolyte having different concentrations. A regulated DC power supply (Physitech electronics, model: PHY8230) in galvanostatic mode (0.2 A/cm^2) was employed to carry out the electrochemical exfoliation. After the complete consumption of the graphite rod (anode), a black precipitate was collected from the electrolyte through centrifugation and subsequently washed with 1 M H_2SO_4 followed by deionized water until the solution becomes neutral pH. The powder was dried at 60 °C for 12 h and used for further studies. The samples prepared in 1 M, 2 M, 3 M, and 4 M KF electrolytes were named as G-M1, G-M2, G-M3, and G-M4, respectively.

Characterization

As prepared EEG samples were characterized using a Renishaw Invia Raman spectrometer with a 532 nm laser as the excitation source. XPS (Thermo Scientific EASCA lab 2000) and FTIR spectroscopy were used to unravel the nature and degree of functionalization along with the change in morphology of these samples. The surface area of the samples was analyzed using Brunauer–Emmett–Teller (BET) adsorption isotherms from a Quantachrome Nova 1200e surface area analyzer. AFM was used to study the thickness of the exfoliated layers.

Electrochemical experiments

All of the electrochemical ORR experiments were carried out in a conventional three-electrode system with a catalyst ink modified GCE as a working electrode, Hg/Hg_2Cl_2 and platinum foil (results were cross-checked with graphite rod counter electrode, too) used as a reference and counter electrodes, respectively. The electrochemical performance of the materials was analyzed using cyclic voltammetry (CV), linear sweep voltammetry (LSV), and rotating ring and disk electrode (RRDE) measurements. A BioLogic SP-300 instrument was used for these controlled experiments and an RRDE with a GC disk (4 mm diameter) and Pt ring (5 mm and 7 mm outer and inner diameters, respectively) electrode was employed for the RRDE-based experiments. The catalyst ink for the electrochemical characterization was prepared by dispersing 10 mg of functionalized graphene in 375 µL of the solvent mixture consisting of isopropyl alcohol (IPA, 275 µL), water (50 µL), and *N*,*N*-dimethyl formamide (DMF, 50 µL). 3 µL and 5 µL of the above-prepared ink was drop cast over the well-polished GCE and RRDE (GCE disk having 4 mm diameter), respectively. All of the electrochemical experiments were carried out in 0.1 M KOH solution (for ORR process) and 0.5 M H_2SO_4 solution (for electrochemical surface area measurements). The 0.1 M KOH electrolyte was initially saturated with ultrahigh pure N_2 followed by O_2 gas before the respective analysis. The details of the calculation for the number of electrons transferred are given in Supporting Information File 1.

The quantification of the H_2O_2 produced was carried out using a UV–vis spectrometer [37,61]. A calibration curve was made using 1 mM $Ce(SO_4)_2$ (25 mL) solution, 1% H_2O_2 solution (30% H_2O_2 solution was diluted to 1%) and the details can be found in Supporting Information File 1 (Figure S9) [61]. Bulk electrolysis was conducted using the above-mentioned inks. In brief, 100 µL of the above-prepared catalyst ink was drop cast over a 1 cm^2 area of the Toray carbon paper having 100 mm length and dried at room temperature. These electrodes were used as working electrodes for bulk electrolysis wherein the electrochemical cell constitutes 100 mL of O_2-saturated 0.1 M KOH electrolyte and a constant potential of 0.358 V vs RHE, applied for 3 h. Subsequently, the sample (3 mL of electrolyte) was collected and used for the quantification of the H_2O_2. The details of the quantification are given in Supporting Information File 1.

Supporting Information

The supporting information includes additional TEM images, a detailed description of the quantification of H_2O_2, deconvoluted XPS spectra of O 1s, AFM analysis, FTIR spectra, ECSA calculations, and RRDE analysis for all EEG samples.

Supporting Information File 1

Additional experimental results and analysis.
[https://www.beilstein-journals.org/bjnano/content/supplementary/2190-4286-11-34-S1.pdf]

Acknowledgements

We thank Prof. Vijayamohanan K. Pillai, IISER Tirupati for his valuable suggestions which helped to improve the quality of the work.

Funding

The authors thank the Tata Institute of Fundamental Research - Hyderabad for the financial support. The authors also acknowledge support from the Department of Atomic Energy, Government of India, under project no. 13/3(13)/2012/TIFR/R&D-II/VoI.IV/6768.

ORCID® iDs

Munaiah Yeddala - https://orcid.org/0000-0001-6241-7897
Tharangattu N. Narayanan - https://orcid.org/0000-0002-5201-7539

References

1. Pesterfield, L. *J. Chem. Educ.* **2009,** *86,* 1182. doi:10.1021/ed086p1182
2. Fukuzumi, S.; Yamada, Y.; Karlin, K. D. *Electrochim. Acta* **2012,** *82,* 493–511. doi:10.1016/j.electacta.2012.03.132
3. Kim, H. W.; Ross, M. B.; Kornienko, N.; Zhang, L.; Guo, J.; Yang, P.; McCloskey, B. D. *Nat. Catal.* **2018,** *1,* 282–290. doi:10.1038/s41929-018-0044-2
4. Campos-Martin, J. M.; Blanco-Brieva, G.; Fierro, J. L. G. *Angew. Chem., Int. Ed.* **2006,** *45,* 6962–6984. doi:10.1002/anie.200503779
5. Iwahama, T.; Sakaguchi, S.; Ishii, Y. *Org. Process Res. Dev.* **2000,** *4,* 94–97. doi:10.1021/op990082f
6. Zhang, J.; Chang, X.; Luo, Z.; Wang, T.; Gong, J. *Chem. Commun.* **2018,** *54,* 7026–7029. doi:10.1039/c8cc03303j
7. Oturan, N.; Oturan, M. A. Electro-Fenton Process: Background, New Developments, and Applications. *Electrochemical Water and Wastewater Treatment;* Elsevier: Amsterdam, Netherlands, 2018; pp 193–221. doi:10.1016/b978-0-12-813160-2.00008-0
8. Rabaey, K.; Rozendal, R. A. *Nat. Rev. Microbiol.* **2010,** *8,* 706–716. doi:10.1038/nrmicro2422
9. Yang, S.; Verdaguer-Casadevall, A.; Arnarson, L.; Silvioli, L.; Čolić, V.; Frydendal, R.; Rossmeisl, J.; Chorkendorff, I.; Stephens, I. E. L. *ACS Catal.* **2018,** *8,* 4064–4081. doi:10.1021/acscatal.8b00217
10. Viswanathan, V.; Hansen, H. A.; Nørskov, J. K. *J. Phys. Chem. Lett.* **2015,** *6,* 4224–4228. doi:10.1021/acs.jpclett.5b02178
11. Feng, Y.; Yang, L.; Liu, J.; Logan, B. E. *Environ. Sci.: Water Res. Technol.* **2016,** *2,* 800–831. doi:10.1039/c5ew00289c
12. Brillas, E.; Mur, E.; Sauleda, R.; Sànchez, L.; Peral, J.; Domènech, X.; Casado, J. *Appl. Catal., B* **1998,** *16,* 31–42. doi:10.1016/s0926-3373(97)00059-3
13. Matsue, T.; Fujihira, M.; Osa, T. *J. Electrochem. Soc.* **1981,** *128,* 2565–2569. doi:10.1149/1.2127292
14. Brillas, E.; Sauleda, R.; Casado, J. *J. Electrochem. Soc.* **1999,** *146,* 4539–4543. doi:10.1149/1.1392671
15. Clerici, M. G.; Ingallina, P. *Catal. Today* **1998,** *41,* 351–364. doi:10.1016/s0920-5861(98)00025-x
16. Ranganathan, S.; Sieber, V. *Catalysts* **2018,** *8,* 379. doi:10.3390/catal8090379
17. Hâncu, D.; Beckman, E. J. *Green Chem.* **2001,** *3,* 80–86. doi:10.1039/b008515o
18. Otsuka, K.; Yamanaka, I. *Electrochim. Acta* **1990,** *35,* 319–322. doi:10.1016/0013-4686(90)87004-l
19. Jiang, Y.; Ni, P.; Chen, C.; Lu, Y.; Yang, P.; Kong, B.; Fisher, A.; Wang, X. *Adv. Energy Mater.* **2018,** *8,* 1801909. doi:10.1002/aenm.201801909
20. Yeddala, M.; Gorle, D. B.; Anbu kulandainathan, M.; Ragupathy, P.; Pillai, V. K. *J. Colloid Interface Sci.* **2019,** *545,* 71–81. doi:10.1016/j.jcis.2019.02.095
21. Rastogi, P. K.; Sahoo, K. R.; Thakur, P.; Sharma, R.; Bawari, S.; Podila, R.; Narayanan, T. N. *Phys. Chem. Chem. Phys.* **2019,** *21,* 3942–3953. doi:10.1039/c8cp06155f
22. Munaiah, Y.; Boopathi, S.; Senthil Kumar, S.; Ragupathy, P. *Mater. Lett.* **2019,** *239,* 184–191. doi:10.1016/j.matlet.2018.12.057
23. Park, J.; Nabae, Y.; Hayakawa, T.; Kakimoto, M.-a. *ACS Catal.* **2014,** *4,* 3749–3754. doi:10.1021/cs5008206
24. Yamanaka, I.; Ichihashi, R.; Iwasaki, T.; Nishimura, N.; Murayama, T.; Ueda, W.; Takenaka, S. *Electrochim. Acta* **2013,** *108,* 321–329. doi:10.1016/j.electacta.2013.06.072
25. Shi, X.; Siahrostami, S.; Li, G.-L.; Zhang, Y.; Chakthranont, P.; Studt, F.; Jaramillo, T. F.; Zheng, X.; Nørskov, J. K. *Nat. Commun.* **2017,** *8,* 701. doi:10.1038/s41467-017-00585-6
26. Campos, M.; Siriwatcharapiboon, W.; Potter, R. J.; Horswell, S. L. *Catal. Today* **2013,** *202,* 135–143. doi:10.1016/j.cattod.2012.05.015
27. Yamanaka, I.; Onizawa, T.; Suzuki, H.; Hanaizumi, N.; Nishimura, N.; Takenaka, S. *J. Phys. Chem. C* **2012,** *116,* 4572–4583. doi:10.1021/jp207679e
28. Chen, S.; Chen, Z.; Siahrostami, S.; Kim, T. R.; Nordlund, D.; Sokaras, D.; Nowak, S.; To, J. W. F.; Higgins, D.; Sinclair, R.; Nørskov, J. K.; Jaramillo, T. F.; Bao, Z. *ACS Sustainable Chem. Eng.* **2018,** *6,* 311–317. doi:10.1021/acssuschemeng.7b02517
29. Melchionna, M.; Fornasiero, P.; Prato, M. *Adv. Mater. (Weinheim, Ger.)* **2019,** *31,* 1802920. doi:10.1002/adma.201802920
30. Pal, S.; Narayanaru, S.; Kundu, B.; Sahoo, M.; Bawari, S.; Rao, D. K.; Nayak, S. K.; Pal, A. J.; Narayanan, T. N. *J. Phys. Chem. C* **2018,** *122,* 23385–23392. doi:10.1021/acs.jpcc.8b08933
31. Sun, T.; Zhang, G.; Xu, D.; Lian, X.; Li, H.; Chen, W.; Su, C. *Mater. Today Energy* **2019,** *12,* 215–238. doi:10.1016/j.mtener.2019.01.004
32. Munaiah, Y.; Dheenadayalan, S.; Ragupathy, P.; Pillai, V. K. *ECS J. Solid State Sci. Technol.* **2013,** *2,* M3182–M3186. doi:10.1149/2.024310jss
33. Munaiah, Y.; Suresh, S.; Dheenadayalan, S.; Pillai, V. K.; Ragupathy, P. *J. Phys. Chem. C* **2014,** *118,* 14795–14804. doi:10.1021/jp503287r
34. Vineesh, T. V.; Nazrulla, M. A.; Krishnamoorthy, S.; Narayanan, T. N.; Alwarappan, S. *Appl. Mater. Today* **2015,** *1,* 74–79. doi:10.1016/j.apmt.2015.09.002
35. Vineesh, T. V.; Kumar, M. P.; Takahashi, C.; Kalita, G.; Alwarappan, S.; Pattanayak, D. K.; Narayanan, T. N. *Adv. Energy Mater.* **2015,** *5,* 1500658. doi:10.1002/aenm.201500658
36. Kumar, M. P.; Raju, M. M.; Arunchander, A.; Selvaraj, S.; Kalita, G.; Narayanan, T. N.; Sahu, A. K.; Pattanayak, D. K. *J. Electrochem. Soc.* **2016,** *163,* F848–F855. doi:10.1149/2.0541608jes
37. Lu, Z.; Chen, G.; Siahrostami, S.; Chen, Z.; Liu, K.; Xie, J.; Liao, L.; Wu, T.; Lin, D.; Liu, Y.; Jaramillo, T. F.; Nørskov, J. K.; Cui, Y. *Nat. Catal.* **2018,** *1,* 156–162. doi:10.1038/s41929-017-0017-x
38. Kong, X.-K.; Chen, C.-L.; Chen, Q.-W. *Chem. Soc. Rev.* **2014,** *43,* 2841–2857. doi:10.1039/c3cs60401b

39. Wu, J.; Ma, L.; Yadav, R. M.; Yang, Y.; Zhang, X.; Vajtai, R.; Lou, J.; Ajayan, P. M. *ACS Appl. Mater. Interfaces* **2015,** *7,* 14763–14769. doi:10.1021/acsami.5b02902
40. Zheng, B.; Wang, J.; Wang, F.-B.; Xia, X.-H. *Electrochem. Commun.* **2013,** *28,* 24–26. doi:10.1016/j.elecom.2012.11.037
41. Boopathi, S.; Narayanan, T. N.; Senthil Kumar, S. *Nanoscale* **2014,** *6,* 10140–10146. doi:10.1039/c4nr02563f
42. Munaiah, Y.; Ragupathy, P.; Pillai, V. K. *J. Electrochem. Soc.* **2016,** *163,* A2899–A2910. doi:10.1149/2.0321614jes
43. Yeddala, M.; Narayanan, T. N.; Pitchai, R.; Pillai, V. K. *ChemistrySelect* **2019,** *4,* 11385–11393. doi:10.1002/slct.201902114
44. Zhong, R.-S.; Qin, Y.-H.; Niu, D.-F.; Tian, J.-W.; Zhang, X.-S.; Zhou, X.-G.; Sun, S.-G.; Yuan, W.-K. *J. Power Sources* **2013,** *225,* 192–199. doi:10.1016/j.jpowsour.2012.10.043
45. Liu, A.; Li, W.; Jin, H.; Yu, X.; Bu, Y.; He, Y.; Huang, H.; Wang, S.; Wang, J. *Electrochim. Acta* **2015,** *177,* 36–42. doi:10.1016/j.electacta.2015.03.166
46. Kakaei, K.; Balavandi, A. *J. Colloid Interface Sci.* **2017,** *490,* 819–824. doi:10.1016/j.jcis.2016.12.011
47. Qiao, X.; Liao, S.; Wang, G.; Zheng, R.; Song, H.; Li, X. *Carbon* **2016,** *99,* 272–279. doi:10.1016/j.carbon.2015.12.034
48. Zhao, J.; Cabrera, C. R.; Xia, Z.; Chen, Z. *Carbon* **2016,** *104,* 56–63. doi:10.1016/j.carbon.2016.03.013
49. Zhao, K.; Su, Y.; Quan, X.; Liu, Y.; Chen, S.; Yu, H. *J. Catal.* **2018,** *357,* 118–126. doi:10.1016/j.jcat.2017.11.008
50. Sun, X.; Zhang, Y.; Song, P.; Pan, J.; Zhuang, L.; Xu, W.; Xing, W. *ACS Catal.* **2013,** *3,* 1726–1729. doi:10.1021/cs400374k
51. Deng, W.; Fang, Q.; Zhou, X.; Cao, H.; Liu, Z. *RSC Adv.* **2016,** *6,* 20843–20849. doi:10.1039/c5ra26088d
52. Zhang, H.-J.; Li, H.; Li, X.; Zhao, B.; Yang, J. *Int. J. Hydrogen Energy* **2014,** *39,* 16964–16975. doi:10.1016/j.ijhydene.2014.08.093
53. Tarasevich, M. R.; Bogdanovskaya, V. A.; Zagudaeva, N. M. *J. Electroanal. Chem. Interfacial Electrochem.* **1987,** *223,* 161–169. doi:10.1016/0022-0728(87)85257-9
54. Yi, Y.; Weinberg, G.; Prenzel, M.; Greiner, M.; Heumann, S.; Becker, S.; Schlögl, R. *Catal. Today* **2017,** *295,* 32–40. doi:10.1016/j.cattod.2017.07.013
55. Panomsuwan, G.; Saito, N.; Ishizaki, T. *J. Mater. Chem. A* **2015,** *3,* 9972–9981. doi:10.1039/c5ta00244c
56. Bard, A. J.; Faulkner, L. R.; Leddy, J.; Zoski, C. G. *Electrochemical methods: fundamentals and applications;* Wiley: New York, 1980; Vol. 2.
57. Blizanac, B. B.; Ross, P. N.; Marković, N. M. *J. Phys. Chem. B* **2006,** *110,* 4735–4741. doi:10.1021/jp056050d
58. Min, X.; Chen, Y.; Kanan, M. W. *Phys. Chem. Chem. Phys.* **2014,** *16,* 13601–13604. doi:10.1039/c4cp01337a
59. Park, S.; An, J.; Jung, I.; Piner, R. D.; An, S. J.; Li, X.; Velamakanni, A.; Ruoff, R. S. *Nano Lett.* **2009,** *9,* 1593–1597. doi:10.1021/nl803798y
60. Ganguly, A.; Sharma, S.; Papakonstantinou, P.; Hamilton, J. *J. Phys. Chem. C* **2011,** *115,* 17009–17019. doi:10.1021/jp203741y
61. Greenhaus, H. L.; Feibush, A. M.; Gordon, L. *Anal. Chem. (Washington, DC, U. S.)* **1957,** *29,* 1531–1534. doi:10.1021/ac60130a045

License and Terms

The definitive version of this article is the electronic one which can be found at:
doi:10.3762/bjnano.11.34

BEILSTEIN JOURNAL OF NANOTECHNOLOGY

Exfoliation in a low boiling point solvent and electrochemical applications of MoO_3

Matangi Sricharan‡, Bikesh Gupta‡, Sreejesh Moolayadukkam
and H. S. S. Ramakrishna Matte*§

Letter

Address:
Energy Materials Laboratory, Centre for Nano and Soft Matter
Sciences, Jalahalli, Bengaluru 560013, India

Email:
H. S. S. Ramakrishna Matte* - matte@cens.res.in

* Corresponding author ‡ Equal contributors
§ Phone: +91-80-23084264. Fax: +91-80-283820

Keywords:
2-butanone; liquid-phase exfoliation; low-boiling point solvent; molybdenum trioxide (MoO_3); supercapacitors

Beilstein J. Nanotechnol. **2020,** *11,* 662–670.
doi:10.3762/bjnano.11.52

Received: 30 November 2019
Accepted: 27 February 2020
Published: 17 April 2020

This article is part of the thematic issue "Graphene and beyond".

Guest Editor: G. U. Kulkarni

Abstract

MoO_3 is a versatile two-dimensional transition metal oxide having applications in areas such as energy storage devices, electronic devices and catalysis. To efficiently utilize the properties of MoO_3 arising from its two-dimensional nature exfoliation is necessary. In this work, the exfoliation of MoO_3 is carried out in 2-butanone for the first time. The achieved concentration of the dispersion is about 0.57 $mg \cdot mL^{-1}$ with a yield of 5.7%, which are the highest values reported to date. These high values of concentration and yield can be attributed to a favorable matching of energies involved in exfoliation and stabilization of MoO_3 nanosheets in 2-butanone. Interestingly, the MoO_3 dispersion in 2-butanone retains its intrinsic nature even after exposure to sunlight for 24 h. The composites of MoO_3 nanosheets were used as an electrode material for supercapacitors and showed a high specific capacitance of 201 $F \cdot g^{-1}$ in a three-electrode configuration at a scan rate of 50 $mV \cdot s^{-1}$.

Introduction

The advent of graphene has opened a new area of research in the field of two-dimensional materials [1]. The extraordinary properties of graphene have led researchers to look into other layered materials, such as metal dichalcogenides (MoS_2, WS_2, WSe_2), hexagonal boron nitride (h-BN), layered double hydroxides, metal hydroxides ($Ni(OH)_2$, $Co(OH)_2$), metal oxides (MoO_3, WO_3) and phyllosilicates, for various applications in different fields [2-5]. Among the layered materials, molybdenum oxide (MoO_3) has gained special attention because of its numerous applications in electronics, catalysis, electrochemistry, solar cells and gas sensors [6]. Monolayered and few-layered MoO_3 has been reported to have better properties than the bulk material [7]. Thus, it is crucial to exfoliate MoO_3 for improved performance in a variety of applications.

Liquid-phase exfoliation (LPE) has been shown to be an effective technique for obtaining dispersions of two-dimensional materials. It also offers the advantages of low cost and scalability [2]. The LPE process is initiated either by ultrasonic vibrations or shearing in a liquid medium that facilitates the exfoliation. To influence the energies relevant for the exfoliation in aqueous media, additives such as surfactants and polymers are used [8]. However, their removal is quite tedious and the remnants are detrimental for some applications. To alleviate this, LPE has been carried out in organic solvents taking into account the Hansen solubility parameters (HSPs) [9]. To exfoliate MoO_3 in organic solvents without any additives, Coleman et al. have found that *N*-methyl-2-pyrrolidone (NMP), *N*-cyclohexyl-2-pyrrolidone, and dimethylformamide are the best solvents [10]. The high boiling point of these dispersions (bp > 150 °C) restrict the usage in flexible devices along with issue that these solvents are also toxic (NFPA 704 health code above 2 [11]).

There are reports in literature where MoO_3 has been exfoliated in solvents with low boiling point, such as isopropyl alcohol (IPA) [5]. Alternative approaches for obtaining MoO_3 dispersions in low boiling point solvents have also been reported. For instance, Alsaif et al. have exfoliated MoO_3 in mixtures of water and alcohols (methanol, ethanol, IPA) [12]. In these dispersions molybdenum bronze (H_xMoO_3) was formed after exposure to UV radiation, making MoO_3 quasi-metallic rather than semiconducting [13,14]. Thus, it is of highest priority to produce MoO_3 dispersions of high concentrations and yields while maintaining the semiconductor properties of MoO_3.

In an attempt to address the aforementioned issues, we exfoliated MoO_3 in 2-butanone, an environmentally benign solvent (NFPA 704 health code = 1) with low boiling point (bp = 80 °C) for the first time. We obtained MoO_3 concentrations up to 0.57 $mg{\cdot}mL^{-1}$ with a yield of 5.7%. It is noteworthy that, the chemical nature of the MoO_3 dispersions was not altered after exposure to sunlight (UV radiation) for 24 h. The exfoliated MoO_3 was used as electrode material for supercapacitor applications. The specific capacitance values were as high as 221 $F{\cdot}g^{-1}$ at 5 $mV{\cdot}s^{-1}$ with good rate capability and capacitance retention in a three-electrode system.

Experimental

Liquid-phase exfoliation of MoO_3

Bulk molybdenum trioxide (MoO_3) powder was purchased from Sigma-Aldrich (99% purity, 300 mesh) and 2-butanone was procured from Finar Limited (AR, 98% purity). All materials were used without further purification. Bulk MoO_3 powder suspensions with different initial concentrations of 5, 7.5, 10, and 20 $mg{\cdot}mL^{-1}$ were sonicated with a probe sonicator Vibra cell VCX 750. All exfoliations were carried out at 60% amplitude using a 13 mm diameter horn in a 100 mL cooling cell maintaining the temperature below 20 °C. For comparison, exfoliations in IPA and IPA/H_2O (1:1) were also performed using a similar protocol. After sonication, the dispersions were allowed to rest for 12 h before centrifuging at 500 rpm (REMI Neya-12) for 1 h to remove non-exfoliated flakes. Small aliquots were collected at regular time intervals in order to measure the concentration. The absorbance of the MoO_3 dispersions was recorded using a UV–vis spectrophotometer (Perkin Elmer Lambda 750) in 10 mm quartz cuvettes. The concentrations of dispersions were determined by using thermogravimetric analysis. For this, 4 mL of MoO_3 dispersion was filled in a 5 mL beaker followed by drying off the solvent at 80 °C in a preheated oven. The remaining MoO_3 powder in the beaker was weighed to determine the concentration. The morphology of MoO_3 flakes was characterized using field-emission scanning electron microscopy (FESEM; Tescan Mira3), transmission electron microscopy (TEM; FEI Talos, 200 kV) and atomic force microsopy (AFM; Agilent 5500). Samples for FESEM and AFM were prepared by dripping 10 µL of MoO_3 dispersion (diluted 100 times) onto a Si/SiO_2 (300 nm) substrate while samples for TEM were prepared by dripping 10 µL of the diluted dispersion on a 300 mesh lacey carbon grid. Raman spectra (Horiba LABRam HR) of the MoO_3 layers were recorded using a 532 nm excitation laser. X-ray diffractograms (XRD; Rigaku Smart lab) of the bulk and exfoliated MoO_3 were obtained using a Cu Kα (1.54 Å) X-ray source. The surface potential of MoO_3 dispersions was determined by zeta potential measurements using a Malvern Zetasizer NanoZS. All electrochemical measurements were carried out using Autolab PGSTAT302N.

Electrode preparation and electrochemical testing

Three-electrode system: A glassy carbon electrode (GCE, 0.3 cm diameter) as the working electrode, Pt wire as counter electrode and a saturated calomel electrode (SCE) as reference electrode were used for the electrochemical testing of the exfoliated MoO_3 dispersions and its composites. In brief, the GCE was cleaned with a polishing cloth using fine alumina abrasive powders and washed thoroughly in deionized water. The required amount of the dispersion of known concentration was dripped onto the cleaned GCE using a micropipette and dried under ambient conditions. Nafion® was used as the binder. To study the effect of the conducting additive, different ratios of conductive carbon black (CB) were added and sonicated for 15 min to obtain homogeneous dispersions, which were then dripped on the GCE. All electrochemical measurements were performed in 1 M H_2SO_4 electrolyte.

Two-electrode system: The optimized ratio obtained from measurements of the three-electrode configuration were used to fabricate two-electrode devices. The respective amounts of MoO_3 and carbon black were mixed with 5 wt % of PVDF and stirred overnight in NMP to form a thick paste. The paste was used to make a thin electrode film on carbon paper (1.5 cm × 1.5 cm) and dried in an oven at 60 °C. To fabricate two-electrode supercapacitors, two such electrodes were sandwiched between battery-grade steel current collectors, separated by filter paper dipped in 1 M H_2SO_4 electrolyte.

Results and Discussion

LPE assisted by tip sonication is an effective technique to peel off mono- and few-layers from layered bulk materials. In the crystal structure of α-MoO_3 the atoms are connected to layers through distorted edge- and corner-sharing MoO_6 octahedra. The layers are linked through weak out-of-plane van der Waals interactions. For exfoliation of MoO_3, 2-butanone, a low boiling point solvent, was chosen the HSP values of which match well with those of MoO_3 (Supporting Information File 1, Table S1). To study the exfoliation efficiency, different initial concentrations (C_i) of MoO_3 (5, 7.5, 10 and 20 mg·mL^{-1}) were sonicated for 1 h using probe sonication. The UV–vis spectra of the dispersions were collected and the absorbance per unit length (A/l) is shown in Figure 1a. As C_i of the dispersion increases the A/l value also increases. This suggest that with an increase of C_i, the final concentration (C_f) of the dispersion also increases. This is probably due to the larger amount of material available for exfoliation. The inset in Figure 1a shows the C_f of the dispersions as a function of C_i. To understand the impact of the sonication time on C_f, MoO_3 with C_i = 10 mg·mL^{-1} (time-dependent studies with other C_i values are shown in Figure S1, Supporting Information File 1) was sonicated for different periods of time (1, 3, 5, and 7 h). The UV–vis spectra of the dispersions were recorded and are shown in Figure 1c. From Figure 1c, it is evident that as the time of sonication increases the A/l value increases, which indicates that C_f increases with increase in sonication time (a similar trend is also observed for other C_i values (Figure S1, Supporting Information File 1). The maximum C_f of 0.57 mg·mL^{-1} (shown in inset of Figure 1b) with a yield of 5.7% is achieved after sonication for 7 h. It is worth noting that this is the highest concentration and yield of MoO_3 dispersions achieved to date, to the best of our knowledge (Figure 1c). The high concentration and yield can be attributed to a favorable matching of the exfoliation and stabilization energies between the solvent and the MoO_3 nanosheets. It has been theoretically reported that apart from the matching of HSP values, factors such as the structure of the solvent, its bulkiness and its re-orientation on the exfoliated nanosheets are other critical parameters to be considered for efficient exfoliation [15,16]. These theoretical studies were also supplemented with experimental observations where it was demonstrated that the simple addition of a –CH_2 group to a solvent drastically changes the efficiency of the LPE process [17-19]. It is also reported that the exfoliation efficiency of layered materials may differ depending on the bulk precursor. To validate this, the

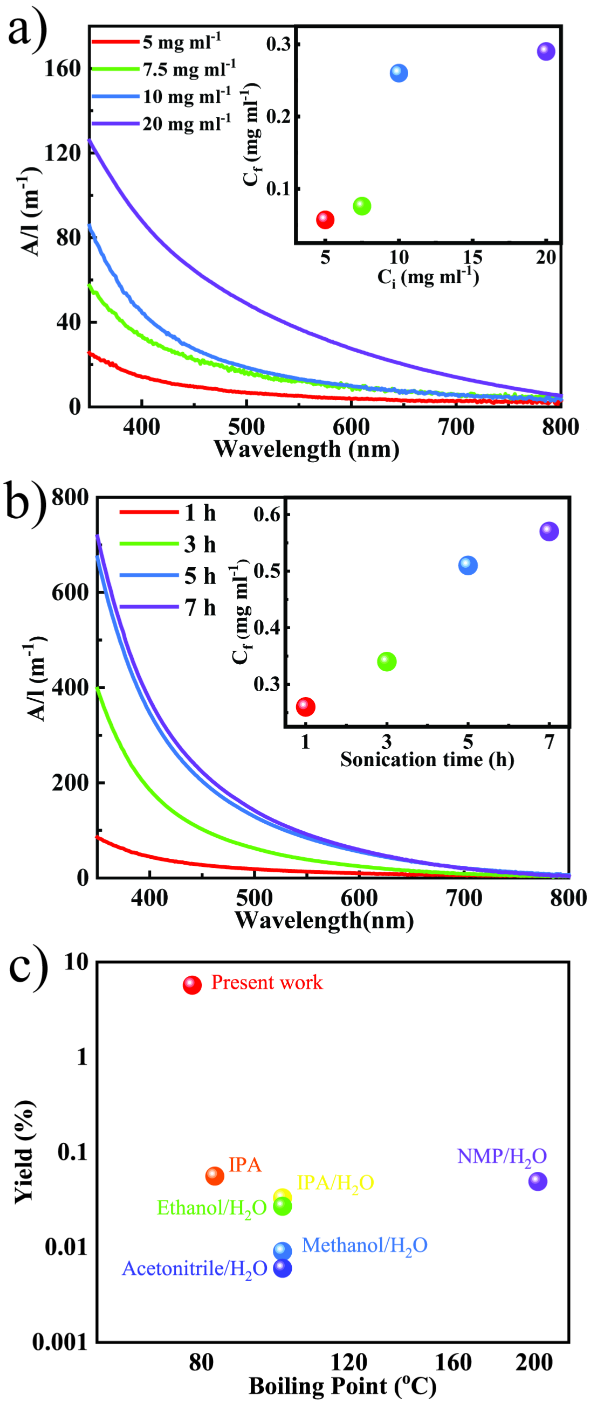

Figure 1: (a) UV–vis spectra of MoO_3 dispersions obtained from different initial concentrations (C_i). The inset shows the final concentration as a function of the initial concentration; (b) UV–vis spectra of MoO_3 dispersions obtained from C_i = 10 mg·mL^{-1} after different sonication durations. The inset shows the final concentration as a function of the sonication time; (c) comparison of previously reported MoO_3 dispersion yields in different solvents [5,12,21].

exfoliation of MoO_3 was carried out from two different precursors procured from different manufacturers. Similar concentrations of MoO_3 dispersions were obtained under identical experimental conditions (Supporting Information File 1, Figure S2) [20].

The structural and chemical nature of the exfoliated MoO_3 nanosheets was determined using microscopic and spectroscopic techniques. The two-dimensional nature of MoO_3 is demonstrated in the TEM micrograph in Figure 2a. Supporting Information File 1, Figure S3c,d, also shows ultrathin nanosheets of MoO_3 suggesting a successful exfoliation. The selected-area electron diffraction (SAED) pattern shown in the inset of Figure 2a indicates that the MoO_3 nanosheets are crystalline after exfoliation. Crystallinity and retention of the orthorhombic phase of exfoliated MoO_3 nanosheets are evident from XRD (Figure S4, Supporting Information File 1). The HRTEM micrograph in Figure 2b shows a *d*-spacing of 0.38 nm corresponding to the (110) planes of orthorhombic MoO_3 (indexed with JCPDS file No. 05-0506). The AFM micrograph in Figure 2c shows the topography of MoO_3 nanosheets the thickness values of which suggest the presence of 5–7 layers [6]. The FESEM micrographs shown in Supporting Information File 1 corroborate the exfoliation of MoO_3. Figure S3a,b (Supporting Information File 1) shows bulk MoO_3 and exfoliated nanosheets of MoO_3, respectively.

Along with the morphological characterization it is also important to assess the chemical nature of the exfoliated nanosheets. It was previously observed that the exfoliation of MoO_3 in some low boiling point alcohols (IPA, ethanol) and mixed solvent systems based on H_2O (IPA/H_2O, ethanol/H_2O) tend to lead to the formation of molybdenum bronze (H_xMoO_3) when exposed to UV radiation [12,21]. The mechanism of the reaction is [13]:

$$MoO_3 \xrightarrow{h\nu} MoO_3 + h^+ + e^-,$$

$$2h^+ + H_2O \longrightarrow 2H^+ + 0.5O_2,$$

$$MoO_3 + xH^+ + xe^- \longrightarrow H_xMoO_3.$$

H^+ ions, which are dissociated from the protic solvents, tend to intercalate in MoO_3 layers forming H_xMoO_3 and the MoO_3 dispersions change the color to blue. It is worth mentioning that exfoliation in 2-butanone did not result in any color change when exposed to sunlight (UV radiation) for 24 h unlike IPA and IPA/H_2O mixture (Figure 2d). The probable reason is the aprotic nature of 2-butanone, which does not support the forma-

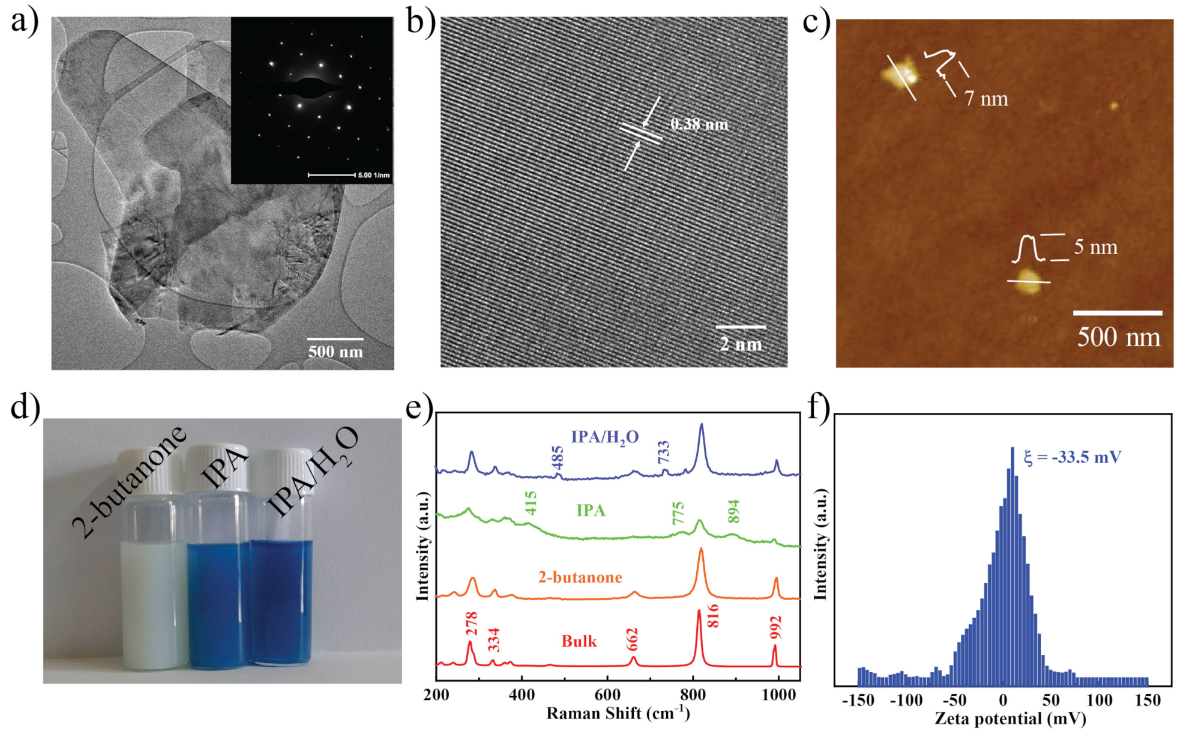

Figure 2: (a) TEM micrograph of MoO_3 nanosheets. The inset shows the SAED pattern; (b) HRTEM micrograph of MoO_3 nanosheets; (c) AFM micrograph of MoO_3 nanosheets; (d) photograph of MoO_3 dispersions in 2-butanone, IPA and IPA/H_2O mixture; (e) Raman spectra of bulk and exfoliated MoO_3 in different solvents; (f) zeta potential of MoO_3 dispersions in 2-butanone.

tion of H^+ in the presence of UV light. This was further confirmed using Raman spectroscopy and UV–vis spectroscopy (Supporting Information File 1, Figure S5). The Raman spectra of bulk and exfoliated MoO_3 in 2-butanone, IPA and an IPA/H_2O mixture are shown in Figure 2e. Bulk and exfoliated MoO_3 in 2-butanone has strong Raman peaks at 278, 334, 662, 816 and 992 cm^{-1}, which are in good agreement with orthorhombic α-MoO_3, suggesting that the exfoliated MoO_3 retained its chemical structure [13]. Additionally, the increase in full width at half maximum (FWHM) from 4 cm^{-1} (bulk) to 8 cm^{-1} (exfoliated in 2-butanone) confirms the exfoliation of MoO_3. However, MoO_3 exfoliated in IPA shows additional peaks at 415, 775 and 894 cm^{-1}, which are due to a deformation of Mo–O bonds confirming the formation of H_xMoO_3 [13]. Similarly, the MoO_3 nanosheets exfoliated in the IPA/H_2O mixture show the evolution of some new peaks at 485 and 733 cm^{-1} suggesting the presence of MoO_{3-x} [13]. The Raman spectra clearly suggest that MoO_3 nanosheets are chemically stable in 2-butanone even after exposure to sunlight. Zeta potential measurements were carried out to determine the charge on the surface of the nanosheets, which is critical for the stability of the dispersions. The high zeta potential of −33.5 mV (Figure 2f) affirms the stability of MoO_3 dispersions in 2-butanone.

Exfoliated two-dimensional materials are known to exhibit good electrochemical properties compared to the bulk materials [22,23]. The electrochemical properties of the exfoliated MoO_3 nanosheets were evaluated using a three-electrode configuration and are shown in Figure 3. Figure 3a shows the cyclic voltammetry (CV) measurement of the electrodes recorded between −0.8 and −0.1 V with a scan rate of 50 mV/s. Initially, pristine exfoliated MoO_3 sheets were studied regarding the charge-storage properties. But, the pristine MoO_3 nanosheets did not show any appreciable currents associated with redox peaks and the calculated specific capacitance was found to be very low (around 2 $F{\cdot}g^{-1}$, Supporting Information File 1, Figure S6). This may be attributed to the poor intrinsic electronic conductivity of the MoO_3 [24]. In order to enhance the electrochemical properties, composites of exfoliated MoO_3 nanosheets and conducting carbon black (CB) were prepared. As shown in Figure 3a, well-defined oxidation and reduction peaks are observed after the addition of 2 wt % CB. The two sets of redox peaks at −0.38 V/−0.47 V and −0.47 V/−0.66 V correspond to the reversible intercalation of the H^+ ions into the MoO_3 layers [25].

In addition, composites were prepared by adding 5 and 8 wt % of CB, and the corresponding CV measurements are shown in Figure 3a. The highest specific capacitance was observed for the composite that contains 5 wt % CB with values reaching up to 221 $F{\cdot}g^{-1}$. The composites with 2 and 8 wt % CB show specific capacitance values of 205 and 149 $F{\cdot}g^{-1}$, respectively, at a scan rate of 5 $mV{\cdot}s^{-1}$. The optimum amount of CB to make conductive pathways in MoO_3 appears to be 5 wt % [26,27]. The change in specific capacitance as a function of the amount of CB is shown in the inset of Figure 3a. The rate capabilities can be understood based on the change in performance as a function of the scan rate [28]. To study this, the composite with 5 wt % CB was cycled at different scan rates (Figure 3b). The change in specific capacitance as a function of the scan rate is shown in Figure 3c. Even at a high scan rate of 50 $mV{\cdot}s^{-1}$ the electrode retained a capacitance value of 200 $F{\cdot}g^{-1}$ suggesting that it is a suitable material for fast-charging applications. This property could be assigned to the two-dimensional nature of the MoO_3 nanosheets, which possess a high surface area allowing for almost unhampered diffusion and electrochemical interaction [29]. To study the effect of exfoliation on the electrochemical properties, bulk MoO_3 with 5 wt % of CB was fabricated and tested under similar conditions. Compared to composites with exfoliated MoO_3 the performance of the composite with bulk MoO_3 is worse (Supporting Information File 1, Figure S6). A comparison of the performance of MoO_3-based supercapacitors is shown in Table S2 (Supporting Information File 1). Galvanostatic charge–discharge measurements are a method to study the charge–discharge characteristics of electrode materials. The composite with 5 wt % CB was charged and discharged at different current densities and pseudocapacitive behavior was observed (Figure 3d). The charge–discharge profile shows a change in slope, which could be due to the electrochemically reversible hydrogen intercalation, which was also seen in the voltammetry curves. The charge and discharge times were found to be 15 and 13 s at a current density of 1 $A{\cdot}g^{-1}$. Cycling stability is a key factor for the commercialization of supercapacitors [30,31]. The composite with 5 wt % CB was tested for about 500 cycles (Figure 3e). Initially the specific capacitance was found to increase, which can be attributed to the wetting of the active material in the initial cycles [26]. Electrochemical impedance spectroscopy was used to study the effect of CB (Figure 3f). The addition of carbon black leads to a reduction of charge transfer resistance in the composites with 5 and 8 wt % CB (6 Ω) compared to the composite with 2 wt % CB (19 Ω). The charge–transfer curve is similar for 5 and 8 wt % CB, which implies that the effect of the additive saturates at 5 wt % CB. This observation also supports the observation from voltammetry data where the composite with 5 wt % CB shows a better performance.

Typically, electrode materials are tested for supercapacitor applications in a three-electrode configuration. But for practical applications, it is appropriate to test them in a two-electrode configuration. The optimized material from the three-electrode

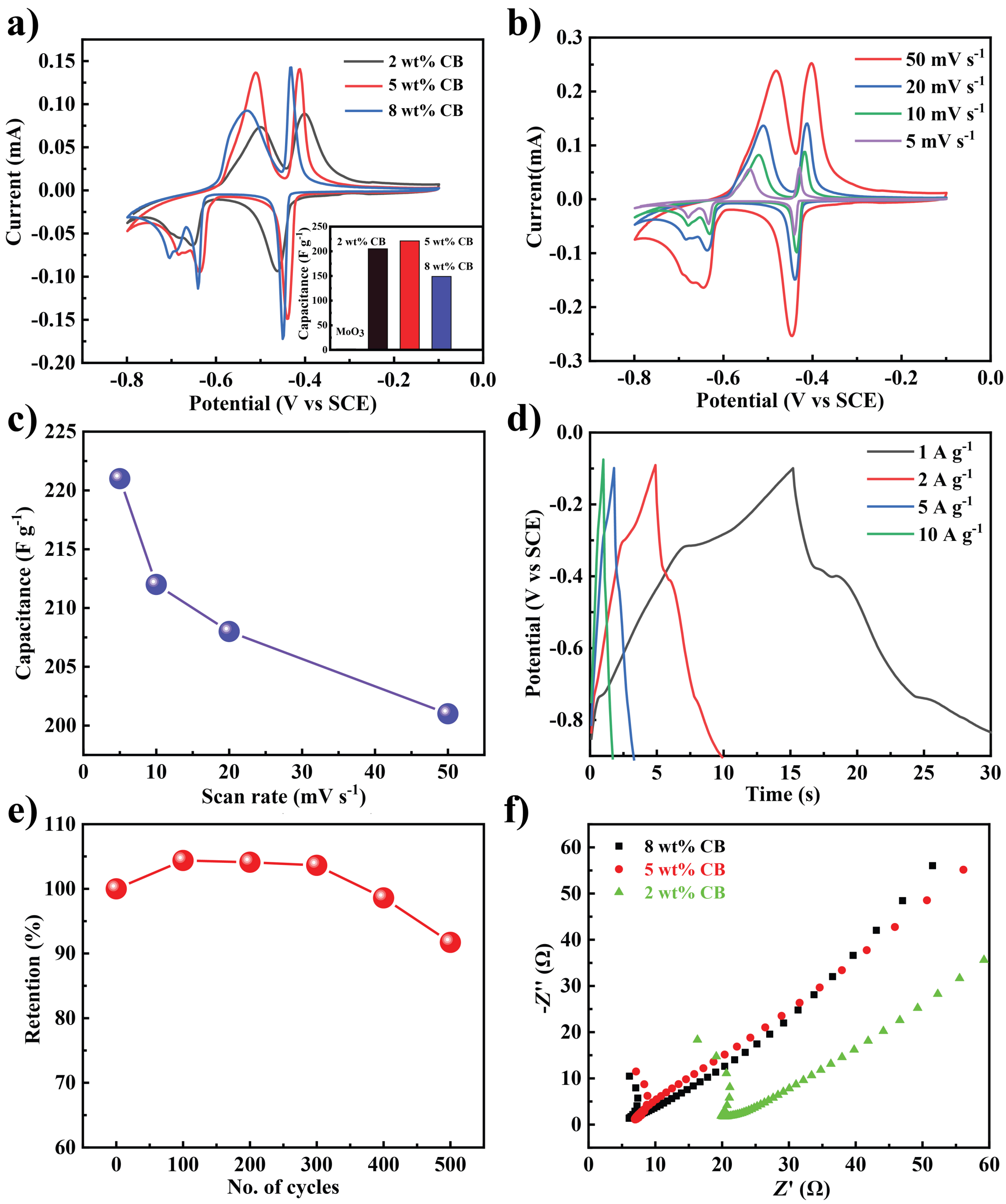

Figure 3: (a) CV measurement of MoO_3/carbon black composites showing pseudo capacitive behavior, inset shows the change in capacitance with increasing mass fraction of carbon black; (b) performance of a composite electrode with 5 wt % CB as a function of the changing scan rate; (c) capacitance as a function of the scan rate, (d) galvanostatic charge–discharge profile of the 5 wt % CB composite; (e) capacitance retention of the 5 wt % CB composite; (f) EIS of the composites.

system (MoO_3/5 wt % CB composite) was chosen for fabricating a two-electrode supercapacitor device (Figure 4). The CV curve of the capacitor at a scan rate of 5 $mV \cdot s^{-1}$ is shown in Figure 4a in a potential window from 0 to 0.6 V. The humps indicating a pseudocapacitance may be attributed to redox reactions in MoO_3 as discussed for the three-electrode measurements. CV measurements have been carried out at different scan rates (Figure 4b). A maximum specific capacitance of 68.4 $F \cdot g^{-1}$ at a scan rate of 5 $mV \cdot s^{-1}$ was obtained. The capacitor also shows good rate capabilities (Figure 4c). The specific capacitance values varied from 18 to 68 $F \cdot g^{-1}$ at scan rates between 50 and 5 $mV \cdot s^{-1}$.

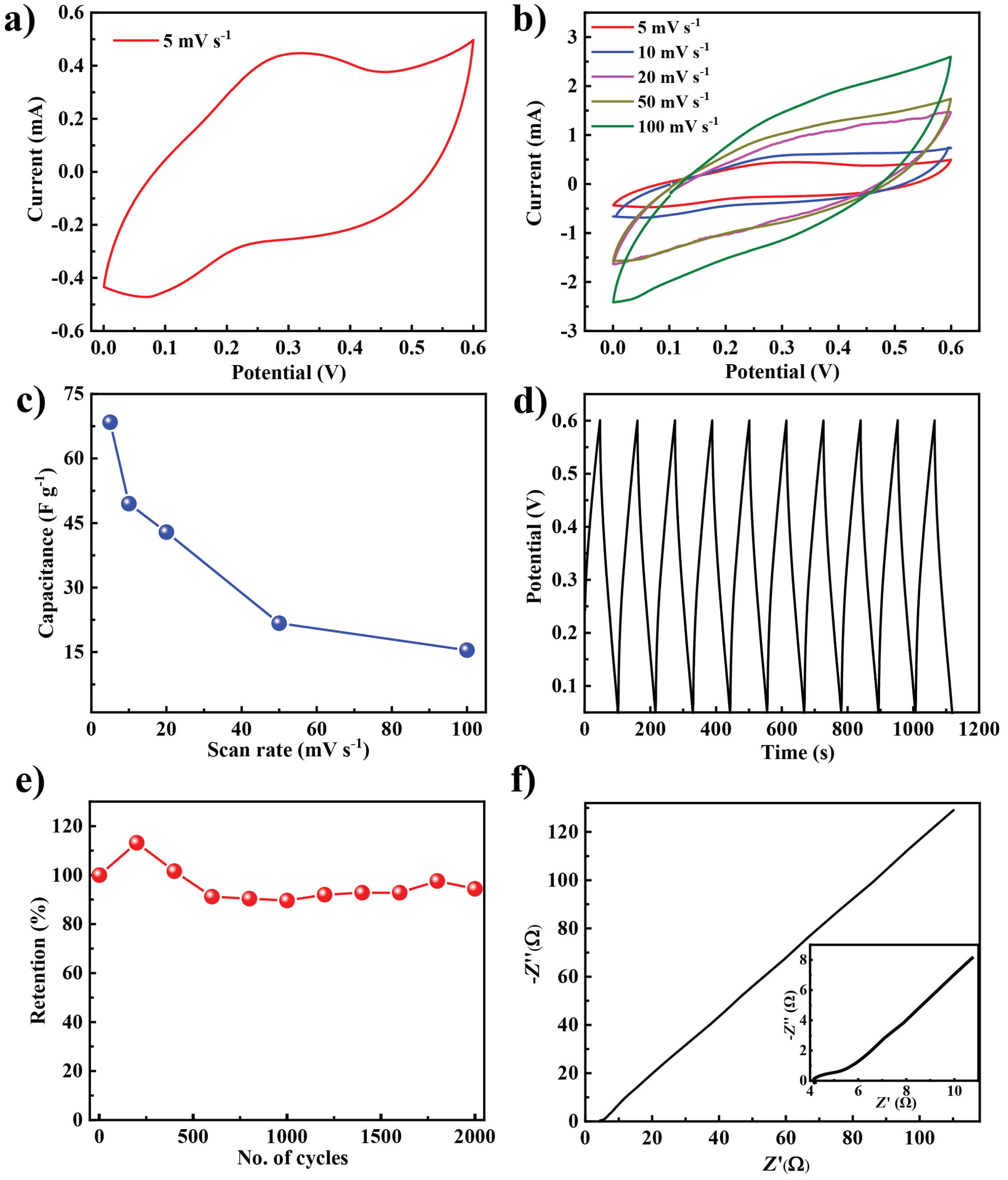

Figure 4: Supercapacitor characterization of a MoO_3/5 wt % CB composite in two-electrode configuration. (a) CV curve of the symmetric capacitor at a scan rate 5 $mV·s^{-1}$; (b) CV curve at different scan rates; (c) capacitance as a function of the scan rate; (d) galvanostatic charge–discharge; (e) cyclic stability and (f) electrochemical impedance spectrum with enlarged view in the inset.

Charge–discharge characteristics of the capacitor are shown in Figure 4d. It shows a capacitive charge–discharge response with a small *iR* drop. This can be attributed to the better conductivity after adding CB. To study the stability of the composite, cyclic voltammetry was carried out up to 2000 cycles. Initially, the capacitance increases, which may be attributed to the wetting of the electrode with the electrolyte and the activation of available sites. Also, the composite shows a capacitance retention up to 94% even after 2000 cycles. Electrochemical impedance spectroscopy (EIS) is used to study the electrochemical series resistance and ideal nature of the capacitor. As shown in Figure 4f, EIS shows a typical plot having a semi-circular loop followed by a straight line. The magnified view in the inset of Figure 4f shows that the composite with 5 wt % CB has a low internal resistance, supporting the observation from the charge–discharge curve.

Conclusion

The exfoliation of MoO_3, carried out in the low boiling point solvent 2-butanone using probe sonication, resulted in a concentration of 0.57 $mg{\cdot}mL^{-1}$ and a yield of 5.7%, which are the highest values reported to date. Additionally, the MoO_3 dispersions in 2-butanone do not undergo any chemical transformation when exposed to sunlight. Composites of the exfoliated MoO_3 nanosheets with carbon black show a high specific capacitance of 201 $F{\cdot}g^{-1}$ at 50 $mV{\cdot}s^{-1}$ in a three-electrode configuration. In a two-electrode configuration, the electrode shows a high stability for 2000 cycles with 94% capacitance retention. We believe the process reported here can be used for the fabrication of flexible supercapacitors for wearable electronics.

Supporting Information

Supporting Information File 1

Additional experimental data.
[https://www.beilstein-journals.org/bjnano/content/supplementary/2190-4286-11-52-S1.pdf]

Acknowledgements

The authors thank Centre for Nano and Soft Matter Sciences (CeNS), Bengaluru for providing all the facilities. The authors thank Mr. Ramesh Chandra Sahoo, CeNS for doing various experiments and proof reading the manuscript.

Funding

HSSRM thanks CeNS for financial support via start-up grant. The authors acknowledge the TEM Facility, funded by a TPF Nanomission, GoI project at CeNS.

ORCID® iDs

Sreejesh Moolayadukkam - https://orcid.org/0000-0002-1046-447X
H. S. S. Ramakrishna Matte - https://orcid.org/0000-0001-8279-8447

References

1. Geim, A. K.; Novoselov, K. S. The rise of graphene. In *Nanoscience and Technology: A Collection of Reviews from Nature Journals;* Rodgers, P., Ed.; World Scientific, 2010; pp 11–19. doi:10.1142/9789814287005_0002
2. Nicolosi, V.; Chhowalla, M.; Kanatzidis, M. G.; Strano, M. S.; Coleman, J. N. *Science* **2013,** *340,* 1226419. doi:10.1126/science.1226419
3. Harvey, A.; He, X.; Godwin, I. J.; Backes, C.; McAteer, D.; Berner, N. C.; McEvoy, N.; Ferguson, A.; Shmeliov, A.; Lyons, M. E. G.; Nicolosi, V.; Duesberg, G. S.; Donegan, J. F.; Coleman, J. N. *J. Mater. Chem. A* **2016,** *4,* 11046–11059. doi:10.1039/c6ta02811j
4. McAteer, D.; Godwin, I. J.; Ling, Z.; Harvey, A.; He, L.; Boland, C. S.; Vega-Mayoral, V.; Szydłowska, B.; Rovetta, A. A.; Backes, C.; Boland, J. B.; Chen, X.; Lyons, M. E. G.; Coleman, J. N. *Adv. Energy Mater.* **2018,** *8,* 1702965. doi:10.1002/aenm.201702965
5. Mendoza-Sánchez, B.; Hanlon, D.; Coelho, J.; O'Brien, S.; Pettersson, H.; Coleman, J.; Nicolosi, V. *2D Mater.* **2016,** *4,* 015005. doi:10.1088/2053-1583/4/1/015005
6. de Castro, I. A.; Datta, R. S.; Ou, J. Z.; Castellanos-Gomez, A.; Sriram, S.; Daeneke, T.; Kalantar-zadeh, K. *Adv. Mater. (Weinheim, Ger.)* **2017,** *29,* 1701619. doi:10.1002/adma.201701619
7. Quek, S. Y.; Biener, M. M.; Biener, J.; Friend, C. M.; Kaxiras, E. *Surf. Sci.* **2005,** *577,* L71–L77. doi:10.1016/j.susc.2005.01.012
8. Coleman, J. N. *Adv. Funct. Mater.* **2009,** *19,* 3680–3695. doi:10.1002/adfm.200901640
9. Coleman, J. N.; Lotya, M.; O'Neill, A.; Bergin, S. D.; King, P. J.; Khan, U.; Young, K.; Gaucher, A.; De, S.; Smith, R. J.; Shvets, I. V.; Arora, S. K.; Stanton, G.; Kim, H.-Y.; Lee, K.; Kim, G. T.; Duesberg, G. S.; Hallam, T.; Boland, J. J.; Wang, J. J.; Donegan, J. F.; Grunlan, J. C.; Moriarty, G.; Shmeliov, A.; Nicholls, R. J.; Perkins, J. M.; Grieveson, E. M.; Theuwissen, K.; McComb, D. W.; Nellist, P. D.; Nicolosi, V. *Science* **2011,** *331,* 568–571. doi:10.1126/science.1194975
10. Hanlon, D.; Backes, C.; Higgins, T. M.; Hughes, M.; O'Neill, A.; King, P.; McEvoy, N.; Duesberg, G. S.; Mendoza Sanchez, B.; Pettersson, H.; Nicolosi, V.; Coleman, J. N. *Chem. Mater.* **2014,** *26,* 1751–1763. doi:10.1021/cm500271u
11. National Fire Protection Association. NFPA 704, Standard System for the Identification of the Hazards of Materials for Emergency Response. 2011; https://www.nfpa.org/codes-and-standards/all-codes-and-standards/list-of-codes-and-standards/detail?code=704 (accessed March 19, 2020).
12. Alsaif, M. M. Y. A.; Field, M. R.; Daeneke, T.; Chrimes, A. F.; Zhang, W.; Carey, B. J.; Berean, K. J.; Walia, S.; van Embden, J.; Zhang, B.; Latham, K.; Kalantar-zadeh, K.; Ou, J. Z. *ACS Appl. Mater. Interfaces* **2016,** *8,* 3482–3493. doi:10.1021/acsami.5b12076
13. Alsaif, M. M. Y. A.; Latham, K.; Field, M. R.; Yao, D. D.; Medehkar, N. V.; Beane, G. A.; Kaner, R. B.; Russo, S. P.; Ou, J. Z.; Kalantar-zadeh, K. *Adv. Mater. (Weinheim, Ger.)* **2014,** *26,* 3931–3937. doi:10.1002/adma.201306097
14. Inzani, K.; Nematollahi, M.; Vullum-Bruer, F.; Grande, T.; Reenaas, T. W.; Selbach, S. M. *Phys. Chem. Chem. Phys.* **2017,** *19,* 9232–9245. doi:10.1039/c7cp00644f
15. Sresht, V.; Pádua, A. A. H.; Blankschtein, D. *ACS Nano* **2015,** *9,* 8255–8268. doi:10.1021/acsnano.5b02683
16. Khan, U.; Porwal, H.; O'Neill, A.; Nawaz, K.; May, P.; Coleman, J. N. *Langmuir* **2011,** *27,* 9077–9082. doi:10.1021/la201797h
17. Lobo, K.; Trivedi, S.; Matte, H. S. S. R. *Nanoscale* **2019,** *11,* 10746–10755. doi:10.1039/c9nr02019e
18. Gupta, B.; Matte, H. S. S. R. *ACS Appl. Electron. Mater.* **2019,** *1,* 2130–2139. doi:10.1021/acsaelm.9b00500
19. Halim, U.; Zheng, C. R.; Chen, Y.; Lin, Z.; Jiang, S.; Cheng, R.; Huang, Y.; Duan, X. *Nat. Commun.* **2013,** *4,* 2213. doi:10.1038/ncomms3213
20. Shen, J.; Wu, J.; Wang, M.; Dong, P.; Xu, J.; Li, X.; Zhang, X.; Yuan, J.; Wang, X.; Ye, M.; Vajtai, R.; Lou, J.; Ajayan, P. M. *Small* **2016,** *12,* 2741–2749. doi:10.1002/smll.201503834
21. Razmyar, S.; Sheng, T.; Akter, M.; Zhang, H. *ACS Appl. Nano Mater.* **2019,** *2,* 4180–4192. doi:10.1021/acsanm.9b00645

22. Sreejesh, M.; Huang, N. M.; Nagaraja, H. S. *Electrochim. Acta* **2015,** *160,* 94–99. doi:10.1016/j.electacta.2015.02.005
23. Wu, S.; Zeng, Z.; He, Q.; Wang, Z.; Wang, S. J.; Du, Y.; Yin, Z.; Sun, X.; Chen, W.; Zhang, H. *Small* **2012,** *8,* 2264–2270. doi:10.1002/smll.201200044
24. Chang, J.; Jin, M.; Yao, F.; Kim, T. H.; Le, V. T.; Yue, H.; Gunes, F.; Li, B.; Ghosh, A.; Xie, S.; Lee, Y. H. *Adv. Funct. Mater.* **2013,** *23,* 5074–5083. doi:10.1002/adfm201301851
25. Tang, W.; Liu, L.; Tian, S.; Li, L.; Yue, Y.; Wu, Y.; Zhu, K. *Chem. Commun.* **2011,** *47,* 10058–10060. doi:10.1039/c1cc13474d
26. Sreejesh, M.; Dhanush, S.; Rossignol, F.; Nagaraja, H. S. *Ceram. Int.* **2017,** *43,* 4895–4903. doi:10.1016/j.ceramint.2016.12.140
27. Shanbhag, D.; Bindu, K.; Aarathy, A. R.; Ramesh, M.; Sreejesh, M.; Nagaraja, H. S. *Mater. Today Energy* **2017,** *4,* 66–74. doi:10.1016/j.mtener.2017.03.006
28. Zhang, L.; Shi, G. *J. Phys. Chem. C* **2011,** *115,* 17206–17212. doi:10.1021/jp204036a
29. Zhou, K.; Zhou, W.; Liu, X.; Sang, Y.; Ji, S.; Li, W.; Lu, J.; Li, L.; Niu, W.; Liu, H.; Chen, S. *Nano Energy* **2015,** *12,* 510–520. doi:10.1016/j.nanoen.2015.01.017
30. Sreedhara, M. B.; Matte, H. S. S. R.; Govindaraj, A.; Rao, C. N. R. *Chem. – Asian J.* **2013,** *8,* 2430–2435. doi:10.1002/asia.201300470
31. Zhou, J.; Lian, J.; Hou, L.; Zhang, J.; Gou, H.; Xia, M.; Zhao, Y.; Strobel, T. A.; Tao, L.; Gao, F. *Nat. Commun.* **2015,** *6,* 8503. doi:10.1038/ncomms9503

License and Terms

The definitive version of this article is the electronic one which can be found at:
doi:10.3762/bjnano.11.52

BEILSTEIN JOURNAL OF NANOTECHNOLOGY

Templating effect of single-layer graphene supported by an insulating substrate on the molecular orientation of lead phthalocyanine

K. Priya Madhuri[1], Abhay A. Sagade*[2], Pralay K. Santra[1] and Neena S. John*[1]

Full Research Paper

Open Access

Address:
[1]Centre for Nano and Soft Matter Sciences, Jalahalli, Bengaluru 560 013, India and [2]Laboratory for Advanced Nanoelectronic Devices, Sir C. V. Raman Research Park, Department of Physics & Nanotechnology, SRM Institute of Science and Technology, Kattankulathur 603 203, Tamil Nadu, India

Email:
Abhay A. Sagade* - abhaya@srmist.edu.in; Neena S. John* - jsneena@cens.res.in

* Corresponding author

Keywords:
conducting atomic force microscopy (C-AFM); lead phthalocyanine (PbPc); molecular orientation; single-layer graphene; substrate effect; two-dimensional grazing incidence X-ray diffraction (2D-GIXRD)

Beilstein J. Nanotechnol. **2020,** *11,* 814–820.
doi:10.3762/bjnano.11.66

Received: 31 January 2020
Accepted: 24 April 2020
Published: 19 May 2020

This article is part of the thematic issue "Graphene and beyond".

Guest Editor: G. U. Kulkarni

Abstract

The influence of single-layer graphene on top of a SiO_2/Si surface on the orientation of nonplanar lead phthalocyanine (PbPc) molecules is studied using two-dimensional grazing incidence X-ray diffraction. The studies indicate the formation of a mixture of polymorphs, i.e., monoclinic and triclinic forms of PbPc with face-on (lying down) and edge-on (standing up) PbPc orientations, respectively. The formation of monoclinic fractions is attributed to the presence of the graphene layer directing the π interactions between the highly delocalized macrocycles. The competing interfacial van der Waals forces and molecule–molecule interactions lead to the formation of a small fraction of triclinic moieties. The nanoscale electrical characterization of the thin PbPc layer on graphene by means of conducting atomic force microscopy shows enhanced vertical conductance with interconnected conducting domains consisting of ordered monoclinic crystallites through which the charge transfer occurs via tunneling. These results show the importance of a templating layer to induce the formation of a required phase of PbPc suitable for specific device applications.

Introduction

Organic semiconductors have been extensively used in, among others, organic light-emitting diodes and organic photovoltaics. In particular, metal phthalocyanines (MPcs) have gained considerable interest as they offer flexibility in the modification of their optoelectronic properties through their molecular packing, which in turn is governed by substrate–molecule interactions [1-4]. Nonplanar MPcs, such as lead phthalocyanine (PbPc), are particularly interesting in the field of photovoltaics due to their extraordinary near-infrared (NIR) absorption. The chemical structure of a PbPc molecule is given in Figure 1. The well-known polymorphs of crystalline nonplanar MPcs are monoclinic and triclinic forms [5]. In thin films of MPcs, the molecules may attain face-on or edge-on orientations with respect to the substrate plane while forming the above crystal phases. The monoclinic fractions are known to have strong absorption in the visible range while the triclinic polymorph exhibits intense NIR absorption bands [3,6]. The formation of specific crystalline phases of nonplanar MPc molecules has been largely explored by introducing various substrate modifications or templating layers including 1*H*,1*H*,2*H*,2*H*-perfluorodecyltrichlorosilane (FDTS), MoO_3 and CuI. A FDTS layer induces the edge-on arrangement regardless of the crystal phase, while a CuI interlayer induces the formation of triclinic PbPc moieties stacked face-on to the substrate yielding enhanced NIR absorption [6]. Organic molecules such as pentacene, fullerene and sexithiophene have also been utilized for inducing the growth of the triclinic phase [7,8]. These studies indicate that the growth of an organic film depends on the delicate interplay between the substrate–molecule and the molecule–molecule interactions. In the case of CuPc molecules deposited on C_{60} layers on highly oriented pyrolytic graphite (HOPG) or SiO_2, it has been reported that CuPc attains different orientations resulting in substantial differences in donor–acceptor energy level alignment at the interface. Thus, ordering and orientation of these molecules significantly affect charge carrier injection and transport in semiconductor devices [7].

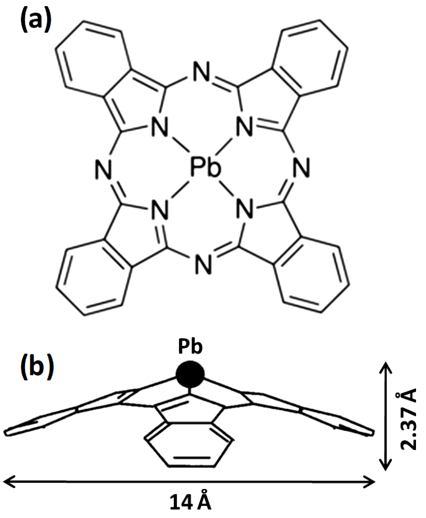

Figure 1: Chemical structure of lead phthalocyanine. (a) Top view and (b) side view of a Pb(II)Pc molecule.

Pristine substrate surfaces of HOPG and Si themselves can induce orientation control over the growth of MPc structures without the aid of additional templating layers. In our earlier work, we have observed that orientation and molecular packing of nonplanar PbPc molecules are influenced by the nature of the substrate, which has been attributed to different substrate–molecule interactions [9]. With the application of 2D materials, such as graphene in device configurations, it is important to understand the orientation of MPc molecules on these atomically thin materials [10,11]. A single-layer of graphene can serve as a transparent conducting electrode and function as donor or acceptor when combined with suitable organic counterparts [12,13]. However, graphene itself is supported on a rigid substrate for device integration and, hence, it is important to consider any influence of the underlying substrate on the MPc orientation. It has been shown that a monolayer of graphene, due to its extremely thin nature, exhibits transparency to the wetting behavior on substrates where van der Waals forces are the dominant surface–water interactions [14]. The wetting transparency disappears with an increasing number of graphene layers, and the wettability approaches that of graphite. The underlying support substrate is reported to even influence the chemical reactivity of a monolayer of graphene [15].

Most of the orientation studies of MPc on graphene deal with planar MPc molecules such as FePc, CoPc, CuPc and ZnPc, which form layers in a face-on configuration [16-19]. A combination of brilliant synchrotron radiation and a highly sensitive 2D X-ray detector are employed to establish the structure and orientation of organic molecules such as MPcs, pentacene and P3HT [6,11,20-22]. Studies concerning the orientation of nonplanar MPcs on graphene are rare. Vanadyl phthalocyanine (VOPc) has been reported to attain edge-on configuration on a graphene surface [23]. The nucleation of CuPc on graphene is reported to be influenced by the underlying Ir(111) substrate [24]. It will be interesting to explore the molecular orientation of nonplanar PbPc on single-layer graphene supported on a substrate. In this study, we have investigated the molecular orientation of a PbPc film deposited on chemical vapor deposition (CVD)-grown graphene transferred onto a SiO_2/Si substrate, using synchrotron two-dimensional grazing incidence X-ray diffraction (2D-GIXRD). We show that although graphene induces the face-on stacking of monoclinic domains, the underlying SiO_2 substrate can still cause edge-on triclinic orientations as well. We also present the electrical current mapping of PbPc on graphene revealing interconnected highly conducting domains.

Results and Discussion

The Raman spectrum of CVD-grown single-layer graphene transferred onto a SiO_2/Si substrate (referred to as SLG/SiO_2/Si hereafter) is presented in Figure 2. A sharp and strong peak at 2680 cm^{-1} corresponds to the characteristic 2D band of SLG and can be fitted with a single Lorentzian function (FWHM =

35.47 cm^{-1}). The peaks at 1587 and 1342 cm^{-1} correspond to the G- and the D-band, respectively [25].

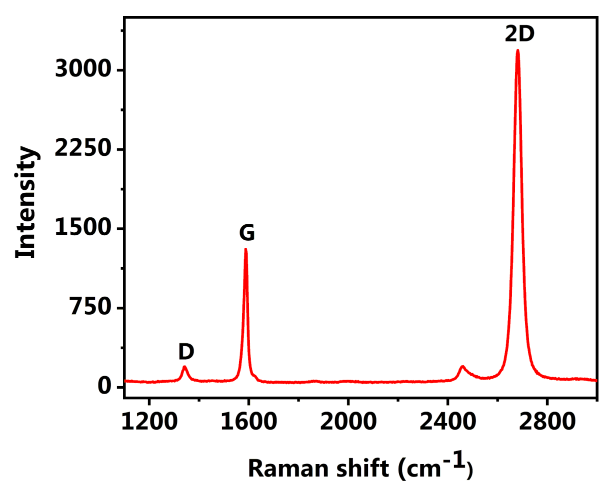

Figure 2: Raman spectrum of single-layer graphene on a SiO_2/Si substrate used as a template for the deposition of the PbPc film.

The structure of the PbPc film on single-layer graphene was studied using 2D-GIXRD. Figure 3a shows the 2D-GIXRD pattern, which clearly shows a peak along the q_z direction at 0.89 Å^{-1}, d = 7.06 Å, corresponding to the (320) reflection of monoclinic PbPc crystallites. Figure 3b shows the profile section of Figure 3a in q_z direction indicating the Braggs peaks as discussed above. The signature of monoclinic moieties along the q_z direction indicates that the PbPc molecules exhibit ordered stacking, normal to the substrate plane. This type of vertical ordering known as cofacial arrangement can promote charge transport in the vertical direction [6,9,26]. Further, a small fraction of the (320) reflection is measured at an azimuthal angle (Figure 3c). The 2D-XRD also shows the presence of a peak at 0.49 Å^{-1} along the q_z direction, which may be assigned to the (200) reflection of the monoclinic phase or the (001) reflection of the triclinic phase, occurring at the same positions with d = 12.82 Å (Figure 3a,b). This less intense peak indicates that there is a small number of crystallites arranged in an edge-on configuration [26]. There is a peak at 0.53 Å^{-1} corresponding to the (100) reflection of the triclinic phase in the q_{xy}

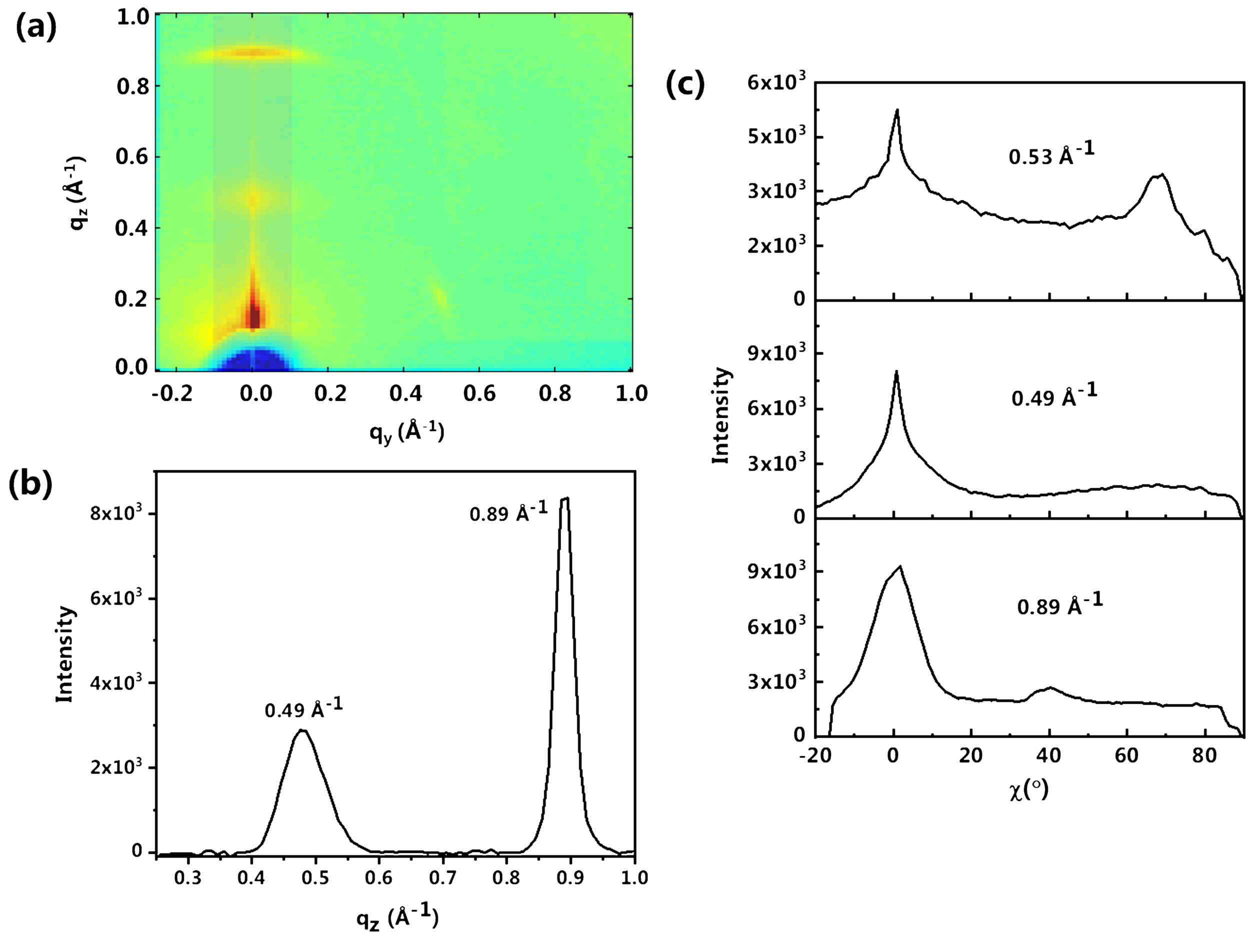

Figure 3: (a) 2D-GIXRD pattern of a 10 nm PbPc film on SLG/SiO_2/Si. (b) Profile section along the q_z direction. (c) Intensity as a function of the azimuthal angle for different Bragg peaks.

plane with $d = 11.87$ Å. This signature in the q_{xy} plane may be an indication of a tilted face-on arrangement of triclinic moieties with respect to the substrate (Figure 3b,c). The average ratio between monoclinic and triclinic phase was roughly estimated from the corresponding Bragg peaks, and the monoclinic phase constitutes 65–70% of the PbPc crystallites.

The molecular orientation of both planar and nonplanar MPc molecules on oxide substrates such as SiO_2 is well known. The molecules were shown to preferably have an edge-on orientation [3,7,9,27-29]. In our earlier studies, we have reproducibly obtained different crystallites of PbPc on substrates such as HOPG, Au(111), Si and SiO_2. Detailed studies using Raman spectroscopy and 2D-GIXRD show ordered monoclinic and triclinic moieties on HOPG and Si substrates, respectively, while the Au(111) surface gives rise to disordered fractions due to the absence of long-range ordering [9,26]. In the present study, the presence of single-layer graphene on SiO_2 has a templating effect and induces a monoclinic packing of PbPc in the face-on configuration. Our previous theoretical studies have shown that the PbPc molecule exclusively adopts a face-on configuration on an unsupported graphene layer owing to π–π and van der Waals interactions. For multilayer depositions, ordered π stacking of the macrocycles with Pb-up configuration is expected due to the dominant π–π interactions between the Pc macrocycle and the graphene layer [9,26].

In the present study, although there is a graphene layer, triclinic moieties with edge-on configuration are still observed. In the case of CVD graphene transferred on to substrates by the polymer method, it has been reported that the presence of polymer residues can cause edge-on orientation for pentacene on graphene [11]. However, in this work, effort has been taken to remove any polymer residues via thermal treatment [30]. Recently, Rafiee et al. found, in the context of wetting, that the van der Waals forces are not disrupted by the graphene sheet as it is extremely thin (ca. 0.3 nm) [14]. Hence, we consider that the edge-on configurations are formed under the influence of the underlying SiO_2. The presence of triclinic moieties in an inclined configuration could be a result of competing interfacial van der Waals and forces and the π interactions between the graphene layer and the underlying SiO_2. Thus more than one layer of graphene may be required to diminish the weak interfacial van der Waals forces from the SiO_2 substrate [7]. The possibility of interaction between molecules in the top layers further away from the influence of graphene may also cause inclined and random orientations [31]. Based on the 2D-GIXRD measurements, a schematic of the molecular arrangement of PbPc molecules with monoclinic and triclinic fractions on the surface of SLG/SiO_2/Si is inferred in Figure 4.

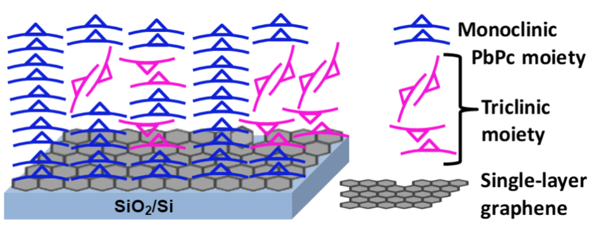

Figure 4: Schematic showing the molecular orientation of PbPc molecules on SLG/SiO_2/Si.

The topography of the PbPc layer was studied using atomic force microscopy (AFM, Figure 5). Figure 5a and the inset show that the film consists of granular PbPc crystallites deposited uniformly on the surface of a single-layer graphene sheet. The size of the PbPc grains is 80–100 nm. The figures show that the film is quite continuous and uniform. Figure 5c shows the profile section taken from the inset of Figure 5a indicating the height variations across the film. The rms roughness of the film was found to be 2.82 nm. Wang et al. carried out a similar study by depositing a 10 nm thin ZnPc film on a

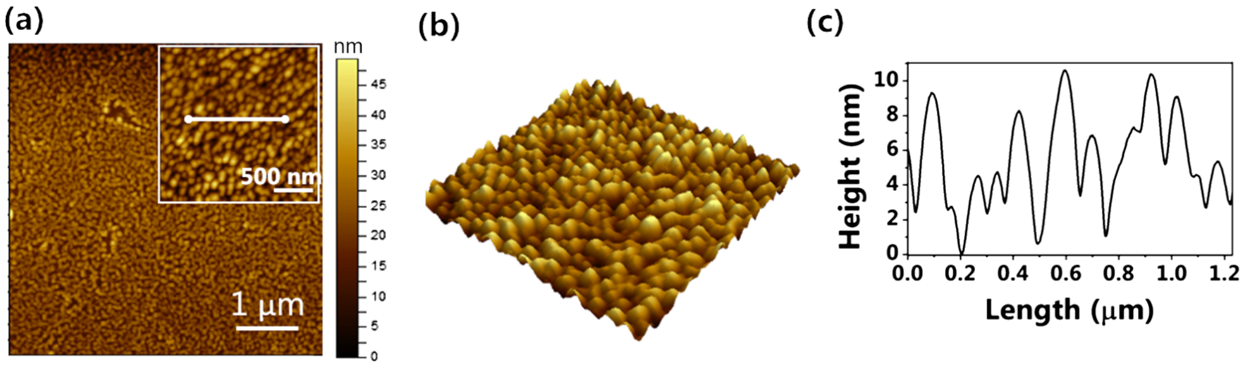

Figure 5: (a) AFM image of a 10 nm PbPc layer on single-layer graphene. The inset shows a magnified image of a 2 µm × 2 µm area. (b) 3D view of the inset image. (c) Profile section across the marked line in the inset of (a) showing the height variation.

graphene/SiO_2/Si substrate to study the effects of the molecular orientation on the interfacial electronic properties. The roughness of the film was reported to be 2.47 ± 0.28 nm [19]. The crystallite size of PbPc was also derived from the 2D-GIXRD peaks at 0.49 and 0.89 $Å^{-1}$ using the Scherrer equation with a value of $k = 0.9$ assuming spherical particles. Crystallite sizes of 14.37 and 33.58 nm were obtained from the Bragg peaks of 0.49 and 0.89 $Å^{-1}$, respectively.

Further, we have carried out electrical studies using conducting-AFM (C-AFM). Figure 6a,b shows the topography and the corresponding current map of the film. The current response map shows an average current value of about 1 nA across the surface with highly conducting grains, which exhibit current values as high as 8–9 nA (Figure 6c). The conducting domains may arise as a result of face-on monoclinic fractions that are vertically stacked. Such stacked molecules can give rise to more energy states near the bandgap aiding charge transport [9]. The less conductive regions may have triclinic moieties or other crystallite arrangements that do not facilitate charge transport. Figure 6d is the I–V curve acquired from one of the conducting domains in the vertical configuration.

The curve is non-linear as expected for PbPc and higher current values are observed. The obtained I–V plot can be fitted to a generalized Simmons equation indicating that the charge transport in a thin PbPc layer is governed by tunneling (Figure 7). A plot of $\ln(I/V^2)$ as a function of V^{-1} indicates a logarithmic dependence in the low-bias region showing direct tunneling, which transforms into a linear dependence in the high-bias region, suggesting Fowler–Nordheim (F-N) tunneling or injection tunneling. However, it is seen that the transition from direct to F-N tunneling is not a sharp transition. Instead, there is a seemingly linear slope between the two states. A sharp rise in linear current is noticed beyond this region, which corresponds to F-N tunneling [9]. Graphene has similar properties as graph-

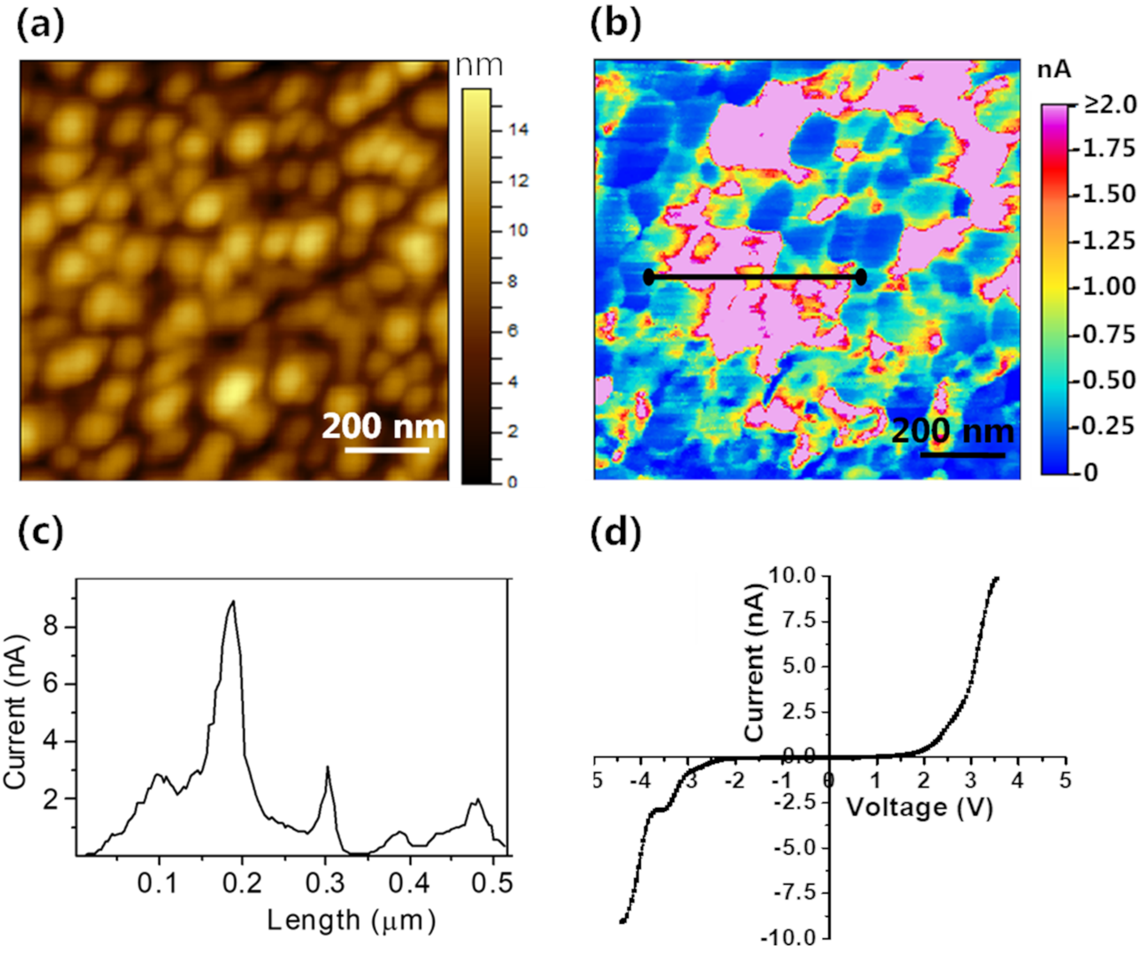

Figure 6: (a) AFM topography,1 µm × 1 µm scan area. (b) Corresponding current map of 10 nm PbPc thin film on SLG/SiO_2/Si substrate obtained at 2 V sample bias. (c) Profile section of (b) along the marked line showing the current variation across the film. (d) I–V curve acquired from a conducting domain.

ite and is expected to exhibit similar templating effects as observed earlier on graphite due to its sp^2-hybridized structure. The vertically stacked monoclinic domains on the graphene surface provide an uninterrupted path for electrical transport and thus give rise to higher current values.

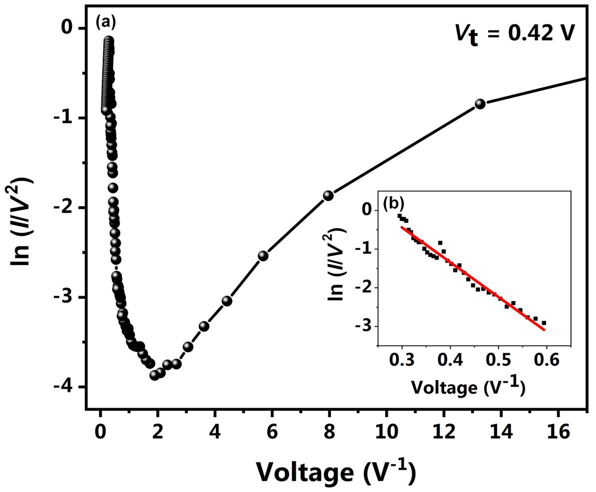

Figure 7: (a) Plot of ln(I/V^2) as a function of V^{-1} for PbPc on single-layer graphene showing a transition from direct tunneling to F-N tunneling and (b) linear fit for the region of F-N tunneling.

Conclusion

Structural studies of a thin layer of PbPc (10 nm) deposited on CVD-grown single-layer graphene supported on a SiO_2/Si substrate show the presence of a mixture of monoclinic and triclinic polymorphs with, respectively, face-on and edge-on configurations. The presence of monoclinic fractions in a preferred face-on orientation is ascribed to the π–π interactions between the sp^2-hybridized plane of graphene and the macrocycles of PbPc. However, the presence of SiO_2 surface beneath graphene, which exerts interfacial van der Waals interactions and intermolecular interactions on the top layers, influences the orientation of PbPc molecules leading to the formation of a very small fraction of triclinic moieties in edge-on or tilted configuration. Further, electrical characterization of these films in a vertical configuration shows enhanced conduction. Monoclinic domains stacked cofacially on the substrate surface facilitate the charge transport by improved π-electron coupling. These studies demonstrate the possibility to fabricate device architectures with the desired orientation of the film by carefully choosing the substrate or introducing a templating layer.

Experimental

A 10 nm thin PbPc film on single-layer graphene supported on a SiO_2/Si substrate (SLG/SiO_2/Si) was deposited using physical vapor deposition. The PbPc film was deposited at a base pressure of 1×10^{-5} mbar while the substrate was held at 100 °C. The deposition rate was 1–1.5 Å·s^{-1}. Single-layer graphene was synthesized by chemical vapor deposition (CVD) on a copper substrate and transferred by a standard technique using poly(methyl methacrylate) (PMMA) onto a SiO_2 (300 nm)/Si substrate as reported elsewhere [30]. This process is optimized with regard to minimal PMMA contamination. Further after the transfer, the substrates were heated to 400 °C in forming gas for 1 h to remove remaining polymer residues.

The structural characteristics of the single-layer graphene were studied using a Horiba XploRA PLUS Raman spectrophotometer with a 532 nm laser and a 50× objective. The molecular orientation of the thermally deposited PbPc film on single-layer graphene was studied using 2D grazing incidence X-ray diffraction (2D-GIXRD) at the PETRA III P08 beamline (Deutsches Elektronen-Synchrotron, DESY) with a flat-panel Perkin Elmer detector with 2048 × 2048 pixels of the size of 200 μm at a beam energy of 25 keV, corresponding to $\lambda = 0.496$ Å. The obtained results were analyzed with the help of the GIXSGUI software with MATLAB interface [32].

Morphological studies and electrical measurements of the PbPc layer were carried out using an Agilent 5500 AFM. The AFM was operated in C-AFM mode in which the PbPc layer is sandwiched between the conductive graphene layer, which served as a bottom electrode, and the Cr/Au tip (diameter < 35 nm and $k = 0.18$ N·m^{-1}, MikroMasch, USA), serving as a top electrode.

Acknowledgements

We acknowledge DESY (Hamburg, Germany), a member of the Helmholtz Association HGF, for the provision of experimental facilities. Parts of this research were carried out at the PETRA III beamline P08. We thank Dr. Florian Bertram at PETRA III for assistance with the 2D-GIXRD experiments.

Funding

DST, India is acknowledged for funding provided within the framework of India@DESY programme. AAS thanks SERB-ECRA (2017/1562) and SRM IST for the financial support.

ORCID® iDs

Abhay A. Sagade - https://orcid.org/0000-0002-3299-7103
Pralay K. Santra - https://orcid.org/0000-0002-1951-5835
Neena S. John - https://orcid.org/0000-0001-6179-2150

References

1. Hohnholz, D.; Steinbrecher, S.; Hanack, M. *J. Mol. Struct.* **2000,** *521,* 231–237. doi:10.1016/s0022-2860(99)00438-x
2. Varotto, A.; Nam, C.-Y.; Radivojevic, I.; Tomé, J. P. C.; Cavaleiro, J. A. S.; Black, C. T.; Drain, C. M. *J. Am. Chem. Soc.* **2010,** *132,* 2552–2554. doi:10.1021/ja907851x

3. Vasseur, K.; Rand, B. P.; Cheyns, D.; Froyen, L.; Heremans, P. *Chem. Mater.* **2011,** *23,* 886–895. doi:10.1021/cm102329v
4. Pearson, A. J.; Plint, T.; Jones, S. T. E.; Lessard, B. H.; Credgington, D.; Bender, T. P.; Greenham, N. C. *J. Mater. Chem. C* **2017,** *5,* 12688–12698. doi:10.1039/c7tc03946h
5. Ottaviano, L.; Lozzi, L.; Phani, A. R.; Ciattoni, A.; Santucci, S.; Di Nardo, S. *Appl. Surf. Sci.* **1998,** *136,* 81–86. doi:10.1016/s0169-4332(98)00315-8
6. Vasseur, K.; Broch, K.; Ayzner, A. L.; Rand, B. P.; Cheyns, D.; Frank, C.; Schreiber, F.; Toney, M. F.; Froyen, L.; Heremans, P. *ACS Appl. Mater. Interfaces* **2013,** *5,* 8505–8515. doi:10.1021/am401933d
7. Wang, C.; Liu, X.; Wang, C.; Xu, X.; Li, Y.; Xie, F.; Gao, Y. *Appl. Phys. Lett.* **2015,** *106,* 121603. doi:10.1063/1.4916559
8. Zhao, W.; Mudrick, J. P.; Zheng, Y.; Hammond, W. T.; Yang, Y.; Xue, J. *Org. Electron.* **2012,** *13,* 129–135. doi:10.1016/j.orgel.2011.10.016
9. Madhuri, K. P.; Kaur, P.; Ali, M. E.; John, N. S. *J. Phys. Chem. C* **2017,** *121,* 9249–9259. doi:10.1021/acs.jpcc.6b09240
10. Huang, H.; Huang, Y.; Wang, S.; Zhu, M.; Xie, H.; Zhang, L.; Zheng, X.; Xie, Q.; Niu, D.; Gao, Y. *Crystals* **2016,** *6,* 113. doi:10.3390/cryst6090113
11. Lee, W. H.; Park, J.; Sim, S. H.; Lim, S.; Kim, K. S.; Hong, B. H.; Cho, K. *J. Am. Chem. Soc.* **2011,** *133,* 4447–4454. doi:10.1021/ja1097463
12. Pang, S.; Hernandez, Y.; Feng, X.; Müllen, K. *Adv. Mater. (Weinheim, Ger.)* **2011,** *23,* 2779–2795. doi:10.1002/adma.201100304
13. Kim, C.-H.; Kymissis, I. *J. Mater. Chem. C* **2017,** *5,* 4598–4613. doi:10.1039/c7tc00664k
14. Rafiee, J.; Mi, X.; Gullapalli, H.; Thomas, A. V.; Yavari, F.; Shi, Y.; Ajayan, P. M.; Koratkar, N. A. *Nat. Mater.* **2012,** *11,* 217–222. doi:10.1038/nmat3228
15. Wang, Q. H.; Jin, Z.; Kim, K. K.; Hilmer, A. J.; Paulus, G. L. C.; Shih, C.-J.; Ham, M.-H.; Sanchez-Yamagishi, J. D.; Watanabe, K.; Taniguchi, T.; Kong, J.; Jarillo-Herrero, P.; Strano, M. S. *Nat. Chem.* **2012,** *4,* 724–732. doi:10.1038/nchem.1421
16. Scardamaglia, M.; Forte, G.; Lizzit, S.; Baraldi, A.; Lacovig, P.; Larciprete, R.; Mariani, C.; Betti, M. G. *J. Nanopart. Res.* **2011,** *13,* 6013–6020. doi:10.1007/s11051-011-0384-1
17. Uihlein, J.; Peisert, H.; Glaser, M.; Polek, M.; Adler, H.; Petraki, F.; Ovsyannikov, R.; Bauer, M.; Chassé, T. *J. Chem. Phys.* **2013,** *138,* 081101. doi:10.1063/1.4793523
18. Xiao, K.; Deng, W.; Keum, J. K.; Yoon, M.; Vlassiouk, I. V.; Clark, K. W.; Li, A.-P.; Kravchenko, I. I.; Gu, G.; Payzant, E. A.; Sumpter, B. G.; Smith, S. C.; Browning, J. F.; Geohegan, D. B. *J. Am. Chem. Soc.* **2013,** *135,* 3680–3687. doi:10.1021/ja3125096
19. Wang, T.; Kafle, T. R.; Kattel, B.; Liu, Q.; Wu, J.; Chan, W.-L. *Sci. Rep.* **2016,** *6,* 28895. doi:10.1038/srep28895
20. Skrypnychuk, V.; Boulanger, N.; Yu, V.; Hilke, M.; Mannsfeld, S. C. B.; Toney, M. F.; Barbero, D. R. *Adv. Funct. Mater.* **2015,** *25,* 664–670. doi:10.1002/adfm.201403418
21. Jeong, J.; Park, S.; Kang, S. J.; Lee, H.; Yi, Y. *J. Phys. Chem. C* **2016,** *120,* 2292–2298. doi:10.1021/acs.jpcc.5b11535
22. Gonzalez Arellano, D. L.; Burnett, E. K.; Demirci Uzun, S.; Zakashansky, J. A.; Champagne, V. K., III; George, M.; Mannsfeld, S. C. B.; Briseno, A. L. *J. Am. Chem. Soc.* **2018,** *140,* 8185–8191. doi:10.1021/jacs.8b03078
23. Marsden, A. J.; Rochford, L. A.; Wood, D.; Ramadan, A. J.; Laker, Z. P. L.; Jones, T. S.; Wilson, N. R. *Adv. Funct. Mater.* **2016,** *26,* 1188–1196. doi:10.1002/adfm.201503594
24. Schwarz, D.; Henneke, C.; Kumpf, C. *New J. Phys.* **2016,** *18,* 023034. doi:10.1088/1367-2630/18/2/023034
25. Ferrari, A. C.; Meyer, J. C.; Scardaci, V.; Casiraghi, C.; Lazzeri, M.; Mauri, F.; Piscanec, S.; Jiang, D.; Novoselov, K. S.; Roth, S.; Geim, A. K. *Phys. Rev. Lett.* **2006,** *97,* 187401. doi:10.1103/physrevlett.97.187401
26. Madhuri, K. P.; Santra, P. K.; Bertram, F.; John, N. S. *Phys. Chem. Chem. Phys.* **2019,** *21,* 22955–22965. doi:10.1039/c9cp03873f
27. Dexters, W.; Bourgeois, E.; Nesládek, M.; D'Haen, J.; Goovaerts, E.; Haenen, K. *Phys. Chem. Chem. Phys.* **2015,** *17,* 9619–9623. doi:10.1039/c5cp00174a
28. Yonehara, H.; Etori, H.; Engel, M. K.; Tsushima, M.; Ikeda, N.; Ohno, T.; Pac, C. *Chem. Mater.* **2001,** *13,* 1015–1022. doi:10.1021/cm000766y
29. Wang, C.; Irfan, I.; Turinske, A. J.; Gao, Y. *Thin Solid Films* **2012,** *525,* 64–67. doi:10.1016/j.tsf.2012.10.065
30. Sagade, A. A.; Aria, A. I.; Edge, S.; Melgari, P.; Gieseking, B.; Bayer, B. C.; Meyer, J. C.; Bird, D.; Brewer, P.; Hofmann, S. *npj 2D Mater. Appl.* **2017,** *1,* 35. doi:10.1038/s41699-017-0037-z
31. Park, B.; Kim, K.; Park, J.; Lim, H.; Lanh, P. T.; Jang, A.-R.; Hyun, C.; Myung, C. W.; Park, S.; Kim, J. W.; Kim, K. S.; Shin, H. S.; Lee, G.; Kim, S. H.; Park, C. E.; Kim, J. K. *ACS Appl. Mater. Interfaces* **2017,** *9,* 27839–27846. doi:10.1021/acsami.7b05129
32. Jiang, Z. *J. Appl. Crystallogr.* **2015,** *48,* 917–926. doi:10.1107/s1600576715004434

License and Terms

BEILSTEIN JOURNAL OF NANOTECHNOLOGY

Microwave-induced electric discharges on metal particles for the synthesis of inorganic nanomaterials under solvent-free conditions

Vijay Tripathi‡, Harit Kumar‡, Anubhav Agarwal and Leela S. Panchakarla*

Full Research Paper

Address:
Department of Chemistry, Indian Institute of Technology Bombay,
Powai, Mumbai 400076, India

Email:
Leela S. Panchakarla* - panchakarla@chem.iitb.ac.in

* Corresponding author ‡ Equal contributors

Keywords:
electric discharges; microwave synthesis; nanomaterials; transmission electron microscopy

Beilstein J. Nanotechnol. **2020,** *11,* 1019–1025.
doi:10.3762/bjnano.11.86

Received: 03 February 2020
Accepted: 22 June 2020
Published: 13 July 2020

This article is part of the thematic issue "Graphene and beyond".

Guest Editor: G. U. Kulkarni

Abstract

Microwave irradiation of metals generates electric discharges (arcs). These arcs are used to generate nanoparticles of Cu and Ni and one-dimensional nanorods of CuS, ZnF_2, and NiF_2 protected with fluorinated amorphous carbon. We have also synthesized reduced graphene oxide and partially rolled graphene by this method.

Introduction

The synthesis of nanomaterials in short time intervals with fewer chemicals has become increasingly important in materials science. Traditional routes of synthesizing nanomaterials, including sol–gel synthesis, solvothermal synthesis, arc-discharge synthesis, or laser ablation, require either large amounts of chemicals or longer synthesis times, or both [1]. Microwave synthesis has become popular in the last three decades as an alternative route for synthesizing molecules and materials at a significantly shorter time scale [2-8]. Dielectric heating under microwave irradiation both in solution and in the solid state rapidly increases the reaction temperature and helps to improve reaction kinetics significantly. This reduces drastically the reaction time [9,10]. Non-thermal effects may also influence the reaction kinetics, which is still a subject of discussion [9,11]. Bulk metals generally reflect microwaves, whereas fine metal powders or thin films can couple with microwaves (the penetration depth of microwaves in metals is 1–2 μm). This will quickly increase the temperature through conduction mechanisms, which enables the sintering of metals by using microwaves [12-14]. It was found that the sintering of metal powders by microwaves produces products that are denser than and mechanically superior to the ones obtained by conventional heating [14]. Other than reflection and conduction, metal particles usually produce electric discharges (arcs) when exposed to microwaves due to the formation of high electric field gradients at sharp edges on the metal surfaces [12]. The generation of arcs might be the reason why microwave irradiation has not been used to generate different nanomaterials from metal particles. However, some studies show that the treatment of metals under microwave irradiation in organic solvents can carbonize the organic solvents forming carbon-coated metallic nanoparticles [15,16]. Recently, Pentsak et al. have shown that metals, such as Cu, Fe, and Mo, on carbon form nanometer-scale structures under microwave heating [17]. However, the microwave discharge technique, which is fast, solvent-free, and easy to set up technically, has not been explored to its fullest potential to synthesize different nanomaterials with controlled morphology.

In this communication, we report on the microwave-induced electric discharge synthesis of Cu, Ni, und Zn nanoparticles from metal particles. Also, we can control the morphology of the nanomaterials, which has not been achieved before. ZnF_2, NiF_2, and CuS nanorods covered with amorphous fluorinated carbon were synthesized. We have also extended this procedure to synthesize reduced graphene oxide and graphene without using any solvents or additional surfactants.

Results and Discussion

Smooth surfaces on commercially available metal particles do not create arcs under microwave irradiation. Instead, they heat up or reflects the microwaves. Thus, activating metal surfaces by acid treatment is essential before using metal particles in further microwave arc experiments. All metal powders were treated with 0.5 M nitric acid under sonication for 10 min to create rough surfaces. In this process, copper partially gets oxidized to Cu_2O. The X-ray diffraction (XRD) patterns show reflections of Cu_2O after acid treatment, while the majority of Cu remains in the metallic form (Figure 1a). Scanning electron microscopy (SEM) images of copper powder before and after acid treatment are shown in Figure 1b and Figure 1c, respectively. The SEM image clearly shows the sharp edges on acid-treated copper. Graphitic carbon nitride (g-C_3N_4) or graphite powder (commercially available) are used as carbon source. g-C_3N_4 is synthesized and characterized according to [18]. X-ray diffraction (XRD) and X-ray photoelectron spectroscopy (XPS) confirms the formation of g-C_3N_4 (Figure S1 in Supporting Information File 1).

The reactions were carried out in quartz or Teflon beakers. A Teflon beaker also served as a carbon and fluorine source for the experiments. Typically, 100 mg of acid-treated metal powder mixed either with graphite powder or g-C_3N_4 (50 mg) were placed inside a domestic kitchen microwave (2.54 GHz, power 700 W) and treated for periods of time between 5 s and 2 min. Arcs were generated in the activated metal, which evaporated the metal along with carbon. Carbon-coated metallic nanoparticles formed on the top lid of the reaction vessel. For synthesizing nanorods, sulfur was used as a growth promoter. Typically, a mixture of activated metal (100 mg), sulfur powder (25 mg) and g-C_3N_4 (50 mg) were added to a Teflon beaker and irradiated with microwaves. It is important to note that in the absence of carbon (graphite/g-C_3N_4), the arc synthesis yielded a mixture of metal and metal oxide nanoparticles and the particle sizes were found to be difficult to control.

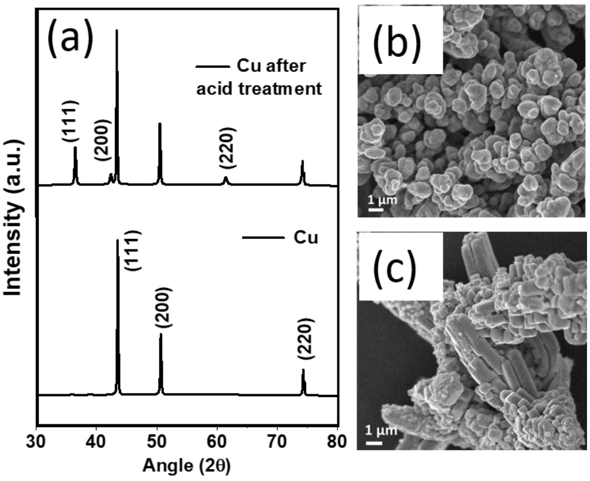

Figure 1: (a) XRD patterns of commercially available Cu powder and Cu powder after treatment with 0.5 M HNO_3. (b) SEM images of pure Cu powder and (c) acid-treated Cu powder.

In Figure 2a, we show a schematic of a reaction vessel inside a microwave device. Figure 2b shows the optical image of plasma generated in the reaction vessel during microwave irradiation. Microwave irradiation of activated metals mixed with either graphite or graphitic carbon nitride (g-C_3N_4) yields carbon-coated or nitrogen-doped carbon-coated metallic nanoparticles. When these reactions are conducted in a Teflon reactor, the products are further functionalized with fluorine. Figure 3a shows XRD patterns of Cu and Ni nanoparticles generated after 1 min of microwave treatment of activated Cu and Ni powders in the presence of g-C_3N_4. The patterns show pure phases of Ni and Cu. The formed nanoparticles are covered with fluorinated amorphous carbon. Figure 3b shows the SEM image of Cu nanoparticles covered with amorphous fluorinated carbon with an average size of 80 nm. The C–F bonds at the surface of the metallic nanoparticles could be further functionalized for different applications such as drug delivery [19]. A SEM image of Ni nanoparticles is shown in Figure S2 in Supporting Information File 1. Figure S3 in Supporting Information File 1 shows the SEM images of Cu nanoparticles covered with amorphous fluorinated carbon synthesized using graphite as carbon source. The structural and morphological features of these Cu nanoparticles are similar to those of Cu nanoparticles produced using g-C_3N_4. In contrast to Cu and Ni, microwave irradiation of zinc metal in

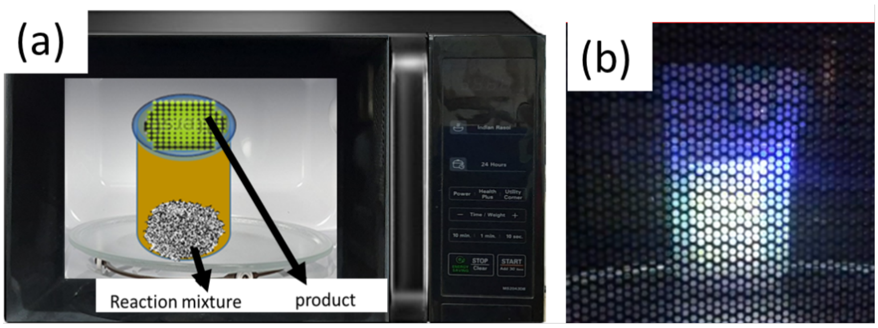

Figure 2: (a) Schematic of the synthesis in a microwave reactor, (b) plasma generated with metal particles under microwave irradiation.

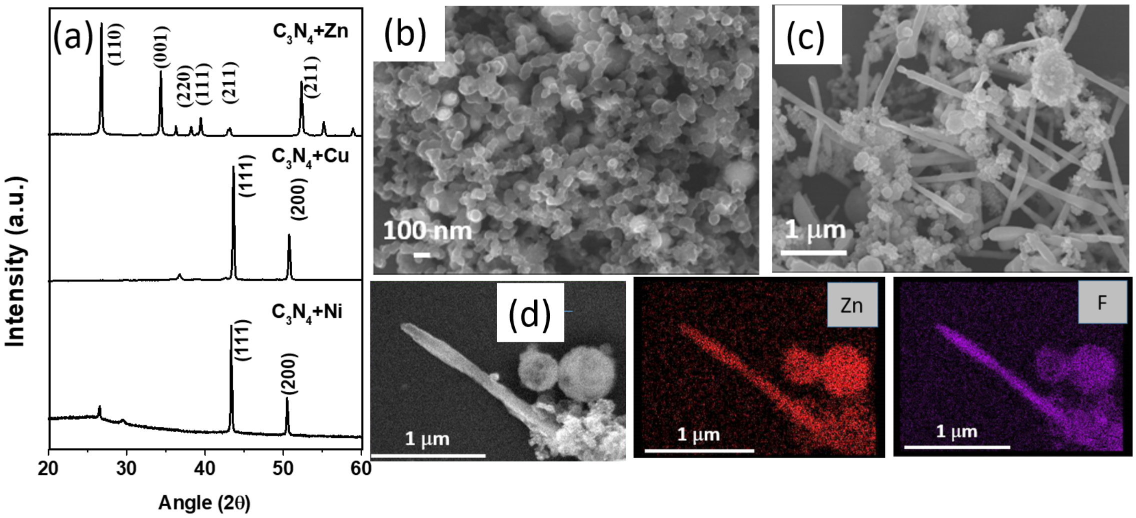

Figure 3: (a) XRD patterns of carbon-coated Cu and Ni nanoparticles and ZnF_2 nanorods. (b) SEM images of carbon-coated Cu nanoparticles. (c) SEM images of ZnF_2 nanorods. (d) SEM image and EDS elemental mapping of a single ZnF_2 nanorod.

the presence of Teflon and g-C_3N_4 creates ZnF_2 nanorods inside fluorinated carbon. From XPS (Figure S4, Supporting Information File 1) the carbon-to-fluorine ratio was calculated to be 3:2. Zn is highly electropositive and reacts readily with fluorine from Teflon and forms ZnF_2. The XRD patterns in Figure 3a confirm the formation of ZnF_2. Both nanorods and nanoparticles of ZnF_2 were formed as can be seen from the SEM image (Figure 3c). Figure 3d shows the energy-dispersive spectroscopy (EDS) mapping of Zn and F, which confirms the presence of Zn and F in the nanorod. The average diameter of the nanorods is 100 nm and the length ranges from 2 to 3 µm. The formation of external amorphous fluorinated carbon nanotubes helps as a template in the formation of ZnF_2 nanorods.

It is well established that sulfur acts as a growth promoter for carbon nanotubes and carbon fibers [20,21]. Thus, sulfur was introduced to the reaction mixtures to improve the yield of nanorods. The microwave treatment of activated Zn metal with g-C_3N_4 and sulfur in a Teflon container produced ZnF_2 nanorods in high yield. The XRD patterns in Figure S5 in Supporting Information File 1 confirm the phase purity of ZnF_2. Figure S6 in Supporting Information File 1 shows the SEM and transmission electron microscopy (TEM) images of ZnF_2 nanorods produced in the presence of sulfur. The SEM images indicate the high yield of ZnF_2 nanorods. The high-resolution TEM (HRTEM) image in Figure S6d (Supporting Information File 1) confirms the single-crystalline nature of ZnF_2. Similarly, microwave treatment of Ni in the presence of sulfur in a Teflon beaker yielded NiF_2 nanorods along with Ni nanoparticles (Figure S5 and Figure S7, Supporting Information File 1). It is important to note that a similar experiment without sulfur yielded only Ni nanoparticles. Figure S7 in Supporting Information File 1 shows SEM and TEM images of NiF_2 nanorods. The EDS mapping in Figure S7c (Supporting Information File 1) confirms the presence of Ni, F and C in the NiF_2 nanorods. A TEM image of NiF_2 nanorod covered with amorphous carbon is shown in Figure S7d (Supporting Information File 1). The HRTEM image (Figure S7e, Supporting Information File 1) clearly shows the single-crystalline nature of the NiF_2 nanorod.

Interestingly, microwave treatment of copper in the presence of sulfur in Teflon yielded CuS nanorods instead of CuF/CuF_2 nanorods. The reactivity of Cu with sulfur is higher than that with fluorine as soft–soft interactions between Cu and S dominate the product stability compared to soft–hard interactions between Cu and F. The XRD pattern in Figure 4a confirms the hexagonal covellite structure of CuS. The SEM image in Figure 4b and the TEM image in Figure 4c confirm the one-dimensional nature. CuS nanorods are single-crystalline as can be seen from the HRTEM image in Figure 4d. CuS nanorods were found to grow along the [101] direction. The average core diameter of the CuS nanorods is about 25 nm and the thickness of the amorphous layer on top of the CuS nanorods is about 5 nm.

Reports on the generation of inorganic nanomaterials from metals by electric arcs under microwave irradiation are rare. Here, we have shown that metals can effectively interact with microwaves when metallic particles contain rough surfaces or sharp edges. When electrically conducting rough surfaces are exposed to microwaves, electric fields distribute inhomogeneously along the surface of the conductor. At tips and sharp edges, very high electric field gradients occur, leading to the ionization of the material and the surrounding gas, followed by electric discharges [12]. These discharges might lead to the melting of the metal and the evaporation of metal, surrounding carbon, sulfur, and fluorine (from Teflon). A chemical reaction between the metal and sulfur and/or fluorine leads to the formation of metal sulfides and/or fluorides depending on the reactivity. Cu and Ni, in the presence of graphite and /or g-C_3N_4 and the absence of sulfur produce metallic nanoparticles. This might be due to the reducing capability of carbon at high temperatures preventing the metals from getting oxidized. When sulfur is used in the reaction mixture along with g-C_3N_4, sulfur helps to produce carbon nanotubes instead of carbon nanospheres. The reactivity of sulfur with the end caps of nanotubes does not allow the carbon nanotubes to close. These amorphous carbon nanotubes help as a template to intercalate metal fluorides/metal sulfides. As the local temperatures are very high, metal fluorides and sulfides melt and fill the nanotubes via capillary forces. The liquids solidify as one-dimensional nanorods inside the nanotubes. The usage of g-C_3N_4, instead of graphite, was found to be beneficial, especially for obtaining high yields of nanorods. However, the choice of

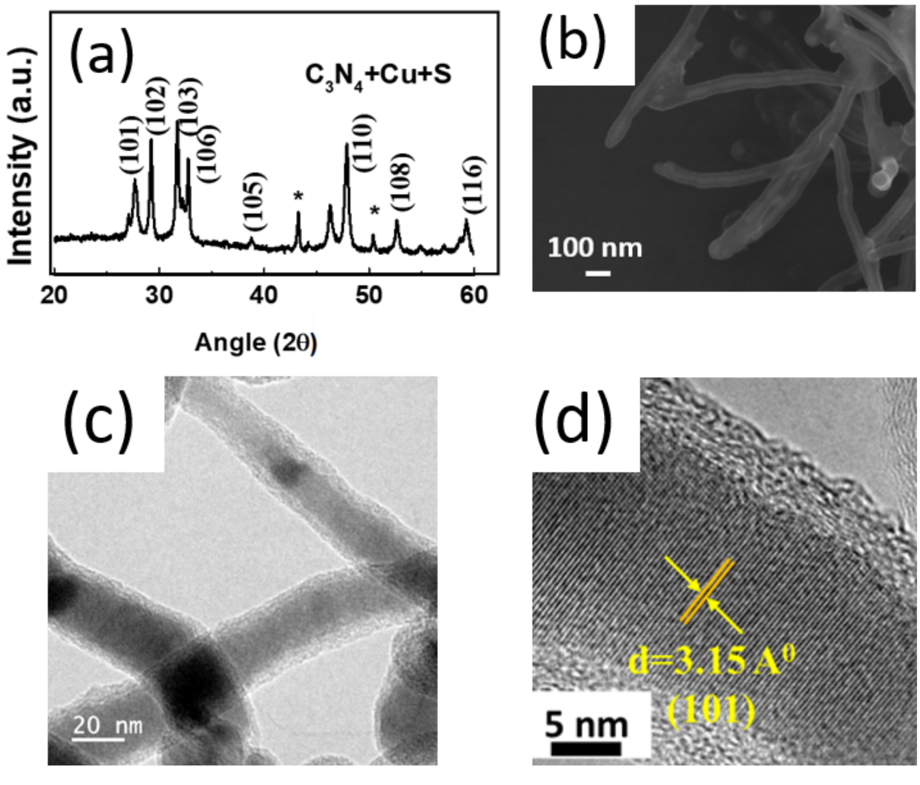

Figure 4: (a) XRD patterns of CuS nanorods synthesized in the presence of sulfur by microwave irradiation of copper in the presence of g-C_3N_4 in a Teflon beaker for 2 min. (b) SEM, (c) TEM and (d) HRTEM images of CuS nanorods. The asterisk (*) in panel (a) indicates the reflections from Cu.

graphite or g-C_3N_4 has shown little to no difference in the synthesis of nanoparticles.

We have also studied exfoliation of graphite and graphite oxide (GO) under microwave irradiation in the presence of Zn metal. We have observed exfoliation of graphite into few-layered graphene. We have also seen a partial rolling of graphene sheets into nanoscrolls (Figure 5a,b). The formation of ultrasmall nanoparticles of ZnO along with graphene was detected (see Figure S8 in Supporting Information File 1). In the case of GO exfoliation, we have observed the formation of nanosheets of reduced graphite oxide (Figure 5c). These nanosheets still keep hexagonal structure under microwave irradiation as can be seen from the selected area electron diffraction pattern in Figure 5d.

Conclusion

We have shown that microwave-induced electric discharges on rough metallic surfaces can be effectively used to synthesize nanomaterials with controlled morphology. Cu and Ni metallic nanoparticles are stabilized through amorphous carbon. Nanorods of ZnF_2, NiF_2 and CuS are synthesized inside fluorinated amorphous carbon nanotubes in the presence of sulfur. External C–F bonds can be further functionalized readily without disturbing internal materials. We could also produce reduced graphene oxide and graphene partially rolled into nanoscrolls. We hope that this work encourages further research exploring the possibilities to synthesize other inorganic nanomaterials by microwave-induced electric discharge without the need for surfactants and solvents.

Experimental

Roughening the surface metal powders

Commercially purchased micrometer-sized metal powders (Ni, Cu and Zn) are treated with nitric acid to create rough surfaces. In a typical reaction, 100 mg of metal powder is transferred to a beaker containing 10 mL of 0.5 M nitric acid and sonicated for 10 min. The resultant powder is washed with water several times until pH 7 and dried it in an oven at 50 °C for 2 h before being used in further microwave experiments.

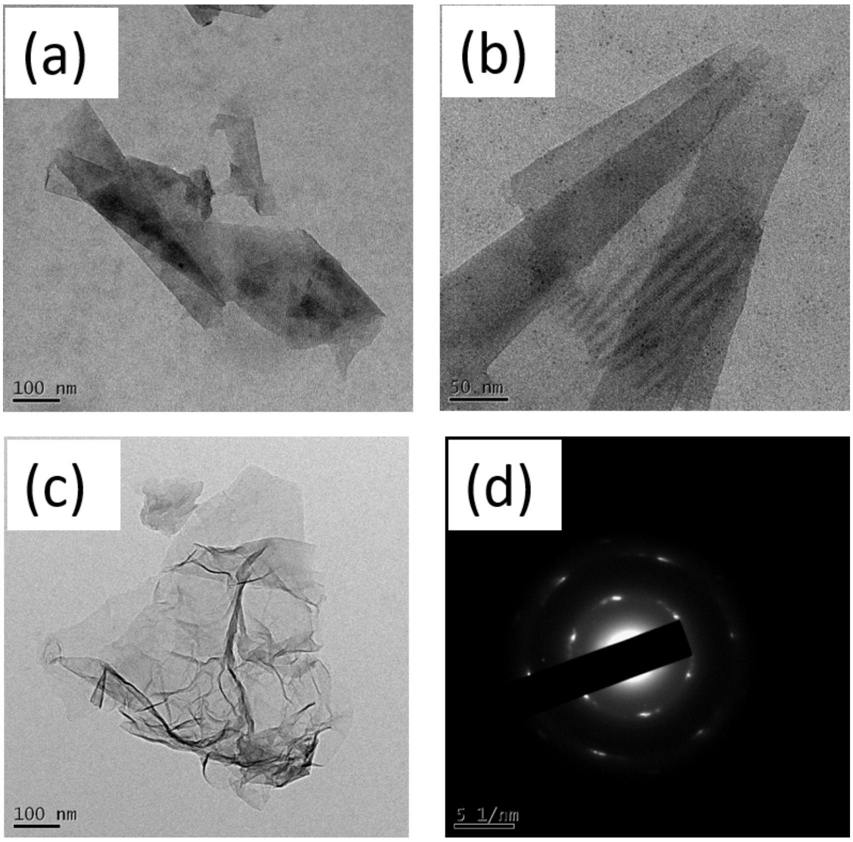

Figure 5: (a, b) TEM images of few-layered graphene partially rolled into nanoscrolls synthesized by irradiating graphite with microwaves in the presence of Zn metal for 30 s. (c) TEM image of graphite oxide after exfoliation trough microwave irradiation in the presence of Zn metal for 30 s and (d) the corresponding selected area electron diffraction pattern.

Synthesis of graphitic carbon nitride (g-C_3N_4)

g-C_3N_4 is synthesized and characterized according to [18]. In a typical reaction, melamine (150 mg) and urea (71 mg) are mixed in a quartz boat and heated at 650 °C under nitrogen flow for 2 h to obtain bulk g-C_3N_4 as orange product.

Generation of nanomaterials using microwave-induced discharge

To generate nanoparticles by microwave-induced discharge, the reaction is conducted either in a quartz or a Teflon beaker. A Teflon beaker also serves as a carbon and fluorine source for the experiments. Typically, 100 mg of acid-treated metal powder mixed either with graphite powder or g-C_3N_4 (50 mg) and placed inside a domestic kitchen microwave (2.54 GHz, power 700 W) and treated for 5 s to 2 min. The product containing carbon-coated metallic nanoparticles are collected from the lid of the reaction vessel. For synthesizing nanorods, sulfur is used as a growth promoter. Typically, a mixture of activated metal (100 mg), sulfur powder (25 mg) and g-C_3N_4 (50 mg) is placed in a Teflon beaker and irradiated with microwaves. The products are collected from the lid of the reaction vessel. The above experiments are performed in air.

Preparation of few-layer graphene and graphite oxide nanosheets

In a typical experiment, 50 mg of acid-treated Zn metal is mixed with 100 mg of either graphite or graphite oxide in a quartz beaker and irradiated with microwaves for 1 min. Products are collected from the reaction vessel, sonicated in ethanol for 1 min and centrifuged for 5 min at 6000 rpm to separate big metal particles and unreacted graphite. The supernatant solution is collected for further characterization.

Characterization of products

The reaction products are characterized by X-ray diffraction (PANanalytical X'pert PRO), field-emission scanning electron microscopy (JEOL JSM 7600F, combined with energy-dispersive spectroscopy (EDS)), transmission electron microscopy (JEOL JEM 2100F) and X-ray photoelectron spectroscopy XPS (Thermo VG Scientific MultiLab, ESCA).

Supporting Information

Supporting Information File 1

Characterization details of g-C_3N_4 by XRD and XPS. Electron microscope analysis of Ni, Cu, ZnF_2, NiF_2, and ZnO nanostructures.
[https://www.beilstein-journals.org/bjnano/content/supplementary/2190-4286-11-86-S1.pdf]

Acknowledgements

Authors acknowledge SAIF, NCPRE and IRCC at IIT Bombay for central facilities.

Funding

LSP acknowledges IIT Bombay and DST-SERB (EMR/2016/003594) for financial support. VT thanks CSIR for a fellowship.

ORCID® iDs

Leela S. Panchakarla - https://orcid.org/0000-0001-5829-3377

Preprint

A non-peer-reviewed version of this article has been previously published as a preprint doi:10.3762/bxiv.2020.14.v1

References

1. Rao, C. N. R.; Müller, A.; Cheetham, A. K., Eds. *The Chemistry of Nanomaterials: Synthesis and Applications;* Wiley-VCH: Weinheim, Germany, 2004. doi:10.1002/352760247x
2. Kitchen, H. J.; Vallance, S. R.; Kennedy, J. L.; Tapia-Ruiz, N.; Carassiti, L.; Harrison, A.; Whittaker, A. G.; Drysdale, T. D.; Kingman, S. W.; Gregory, D. H. *Chem. Rev.* **2014,** *114,* 1170–1206. doi:10.1021/cr4002353
3. Ni, Z.; Masel, R. I. *J. Am. Chem. Soc.* **2006,** *128,* 12394–12395. doi:10.1021/ja0635231
4. Polshettiwar, V.; Varma, R. S. *Acc. Chem. Res.* **2008,** *41,* 629–639. doi:10.1021/ar700238s
5. Mallikarjuna, N. N.; Varma, R. S. *Cryst. Growth Des.* **2007,** *7,* 686–690. doi:10.1021/cg060506e
6. Bilecka, I.; Niederberger, M. *Nanoscale* **2010,** *2,* 1358–1374. doi:10.1039/b9nr00377k
7. Liu, Z.; Wang, J.; Kushvaha, V.; Poyraz, S.; Tippur, H.; Park, S.; Kim, M.; Liu, Y.; Bar, J.; Chen, H.; Zhang, X. *Chem. Commun.* **2011,** *47,* 9912–9914. doi:10.1039/c1cc13359d
8. Bajpai, R.; Wagner, H. D. *Carbon* **2015,** *82,* 327–336. doi:10.1016/j.carbon.2014.10.077
9. Dudley, G. B.; Richert, R.; Stiegman, A. E. *Chem. Sci.* **2015,** *6,* 2144–2152. doi:10.1039/c4sc03372h
10. Ching Lau, C.; Kemal Bayazit, M.; Reardon, P. J. T.; Tang, J. *Chem. Rec.* **2019,** *19,* 172–187. doi:10.1002/tcr.201800121
11. Díaz-Ortiz, Á.; Prieto, P.; de la Hoz, A. *Chem. Rec.* **2019,** *19,* 85–97. doi:10.1002/tcr.201800059
12. Sun, J.; Wang, W.; Yue, Q. *Materials* **2016,** *9,* 231. doi:10.3390/ma9040231
13. Whittaker, A. G.; Mingos, D. M. P. *J. Chem. Soc., Dalton Trans.* **1992,** 2751–2752. doi:10.1039/dt9920002751
14. Roy, R.; Agrawal, D.; Cheng, J.; Gedevanishvili, S. *Nature* **1999,** *399,* 668–670. doi:10.1038/21390
15. Hsin, Y.-L.; Lin, C.-F.; Liang, Y.-C.; Hwang, K. C.; Horng, J.-C.; Ho, J.-a. A.; Lin, C.-C.; Hwu, J. R. *Adv. Funct. Mater.* **2008,** *18,* 2048–2056. doi:10.1002/adfm.200701407
16. Chen, W.; Gutmann, B.; Kappe, C. O. *ChemistryOpen* **2012,** *1,* 39–48. doi:10.1002/open.201100013
17. Pentsak, E. O.; Cherepanova, V. A.; Sinayskiy, M. A.; Samokhin, A. V.; Ananikov, V. P. *Nanomaterials* **2019,** *9,* 19. doi:10.3390/nano9010019

18. Dante, R. C.; Martín-Ramos, P.; Correa-Guimaraes, A.; Martín-Gil, J. *Mater. Chem. Phys.* **2011,** *130,* 1094–1102. doi:10.1016/j.matchemphys.2011.08.041
19. Khabashesku, V. N.; Billups, W. E.; Margrave, J. L. *Acc. Chem. Res.* **2002,** *35,* 1087–1095. doi:10.1021/ar020146y
20. Zhang, L.; Hou, P.-X.; Li, S.; Shi, C.; Cong, H.-T.; Liu, C.; Cheng, H.-M. *J. Phys. Chem. Lett.* **2014,** *5,* 1427–1432. doi:10.1021/jz500419r
21. Suzuki, S.; Mori, S. *Chem. Phys. Lett.* **2018,** *709,* 1–6. doi:10.1016/j.cplett.2018.08.037

License and Terms

The definitive version of this article is the electronic one which can be found at:
doi:10.3762/bjnano.11.86